Nutrient Availability Dictates Cancer Metabolism–Based Therapeutic Responses to Nononcology Drugs

Woo Yang Pyun[1], Jae Hyung Park[1], Jae Won Roh[2], Dongkyu Jeon[3], Jongwan Kim[4,5], Ji Eun Paik[1], Seok Chan Cho[1], So Yeon Park[1], Hocheol Lim[5], Hyungwoo Kim[6], Young Jin Jang[7], Jaehoon Lee[1,8], Jong Hwa Byun[1], Dong Woo Son[1], Soo-Youl Kim[9], Kun-Liang Guan[10], Won Dong Lee[1], Heon Yung Gee[2], Han-Woong Lee[1,8], Kyoung Tai No[4,5], Yu Suk Choi[11], Tadayoshi Hashimoto[12], Takayuki Yoshino[12], Han-Sol Jeong[13], Wan Namkung[3], Joo Hyun Nam[14,15,16], and Hyun Woo Park[1]

ABSTRACT

Metabolic dysregulation is a major hallmark of cancer, making interventions that modify tumor nutrient availability attractive adjuvants for improving clinical outcomes for patients with cancer. Clarifying how the nutritional status of individual patients affects the metabolic vulnerability of tumors to drugs is needed to inform personalized treatment guidelines. Working toward the goal of oncometabolic precision medicine, we developed the cancer metabolism–based synthetic lethality platform (CM-SLP), a high-throughput screening platform that explores the metabolic vulnerability of cancer cells to nononcology drugs induced by altered nutrient availability and predicts potential synthetic lethal interactions with nutrient conditions. Promising CM-SLP candidates included propafenone and biguanides as representative nononcology drugs that cooperatively enhanced cytotoxicity via dysregulated metabolic pathways. Furthermore, the mTOR and Hippo pathways mediated the response to combined propafenone/hypoglycemia or biguanides/hypoglycemia treatments, respectively, and mTOR or TEAD inhibitors circumvented the need for dietary interventions to enhance cancer cell death. Together, these results indicate that CM-SLP represents a promising approach for integrating metabolic profiling into precision oncology, offering therapeutic avenues tailored to individual patient needs.

Significance: A high-throughput screening approach investigating drug vulnerabilities dependent on nutrient status supports repurposing FDA-approved compounds as metabolically informed therapies for next-generation oncometabolic precision medicine.

Introduction

Cancer progression depends on reprogrammed cellular metabolism to support uncontrolled cell proliferation (1). Cancer cells exhibit increased nutrient uptake from the tumor microenvironment and altered intracellular pathways to meet the elevated demand for ATP production and biosynthesis of macromolecules required for rapid cell growth (2). The Warburg effect demonstrates the higher demand of cancer cells for glucose than normal cells, which forms the basis for 2[^{18}F]fluoro-2-deoxy-D-glucose PET/CT imaging of cancer. Because cancer cell metabolism is heavily influenced by systemic and microenvironmental nutrient availability, dietary and pharmacologic interventions that alter cancer metabolism can be used as an adjuvant to standard antineoplastic therapies to improve clinical outcomes (3, 4). The precise mechanisms, however, through which the metabolic vulnerabilities of cancer cells can be systematically exploited remain poorly understood, limiting the translation of these strategies into clinical practice. Addressing this gap is critical for developing innovative approaches to improve patient care and refine individualized treatment regimens.

[1]Department of Biochemistry, College of Life Science and Biotechnology, Brain Korea 21 Four Project, Yonsei University, Seoul, Republic of Korea. [2]Department of Pharmacology, Graduate School of Medical Science, Brain Korea 21 Project, Yonsei University College of Medicine, Seoul, Republic of Korea. [3]College of Pharmacy and Yonsei Institute of Pharmaceutical Sciences, Yonsei University, Incheon, Republic of Korea. [4]Department of Biotechnology, College of Life Science and Biotechnology, Yonsei University, Seoul, Republic of Korea. [5]Bioinformatics and Molecular Design Research Center (BMDRC), Incheon, Korea. [6]Division of Pharmacology, School of Korean Medicine, Pusan National University, Yangsan, Republic of Korea. [7]Major of Food Science and Technology, Seoul Women's University, Seoul, Republic of Korea. [8]Gemcro, Inc., Seoul, Republic of Korea. [9]Division of Cancer Biology, Research Institute, National Cancer Center, Goyang, Republic of Korea. [10]School of Life Sciences, Westlake University, Hangzhou, China. [11]School of Human Sciences, University of Western Australia, Crawley, Australia. [12]Department of Gastroenterology and Gastrointestinal Oncology, National Cancer Center Hospital East, Kashiwa, Japan. [13]Division of Applied Medicine, School of Korean Medicine, Pusan National University, Yangsan, Korea. [14]Department of Physiology, Dongguk University College of Medicine, Gyeongju, Republic of Korea. [15]Channelopathy Research Centre (CRC), Dongguk University College of Medicine, Goyang, Republic of Korea. [16]Department of Physiology, Sungkyunkwan University School of Medicine, Suwon, Republic of Korea.

W.Y. Pyun, J.H. Park, J.W. Roh, and D. Jeon contributed equally to this article.

Corresponding Authors: Han-Sol Jeong, Division of Applied Medicine, School of Korean Medicine, Pusan National University, Yangsan, Gyeongnam 50612, Korea. E-mail: jhsol33@pusan.ac.kr; Wan Namkung, College of Pharmacy and Yonsei Institute of Pharmaceutical Sciences, Yonsei University, Incheon 21983, Republic of Korea. E-mail: wnamkung@yonsei.ac.kr; Joo Hyun Nam, Department of Physiology, Sungkyunkwan University School of Medicine, Suwon 16419, Republic of Korea. E-mail: ferinus@skku.edu; and Hyun Woo Park, Department of Biochemistry, College of Life Science and Biotechnology, Brain Korea 21 Four Project, Yonsei University, Seoul 03722, Republic of Korea. E-mail: hwp003@yonsei.ac.kr

Cancer Res 2026;86:1194–214

doi: 10.1158/0008-5472.CAN-25-1123

Emerging evidence indicates that nutrient availability in the blood or tumor microenvironment of individual patients with cancer significantly influences tumor progression, drug responses, and clinical outcomes (5, 6). In addition, dietary interventions induce differential cytotoxic responses to anticancer drugs in cancer versus normal cells (7). To advance the concept of oncometabolic precision medicine, we developed a cancer metabolism–based synthetic lethality platform (CM-SLP), a high-throughput screening platform designed to explore metabolic vulnerabilities associated with altered nutrient conditions. CM-SLP is the first comprehensive resource to evaluate the synthetic lethality of hyper- or hypo-nutrient states with therapeutic compounds, providing clinically feasible, safe, and effective strategies. Although our study shares conceptual similarity with prior glucose-starvation screens, our study applies a broader approach across diverse nutrient states and focused on repositioning FDA-approved nononcology drugs (8). By screening a panel of 1,813 FDA-approved drugs, CM-SLP identifies unexpected cytotoxic effects arising from altered concentrations of glucose, glutamine, and fatty acids. Our findings reveal that nutrient states differentially sensitize cancer cells, while sparing normal cells, to various drugs prescribed for diverse diseases. Through detailed mechanistic studies, CM-SLP enables the systematic analysis of an individual cancer patient's metabolic profile, offering tailored modifications to treatment regimens to improve clinical outcomes. Furthermore, CM-SLP elucidates the effects of nutrient states on signaling transduction and drug responses, highlighting synthetic lethal interactions between therapeutic compounds and specific metabolites. Moreover, CM-SLP has the potential to mitigate cancer treatment–induced metabolic syndromes, such as diabetes, obesity, and hypertension, by identifying metabolite-dependent cytotoxic side effects associated with various nononcology drugs. Collectively, CM-SLP establishes a framework for personalized treatment regimens that reduce adverse effects while enhancing therapeutic efficacy in patients with cancer with diverse metabolic states. In this study, we validated nononcology drugs, as a candidate with selective activity under nutrient restriction, thereby providing a mechanistic rationale for nutrient–drug synthetic lethality.

Together, CM-SLP presents a comprehensive framework for uncovering metabolite-dependent drug repurposing strategies and emphasizing the importance of evaluating drug responses in the context of nutrient availability. Our findings contribute to the understanding of how metabolic status can influence drug responses, highlighting the potential of incorporating patient-specific metabolic profiles into more tailored therapeutic approaches.

Materials and Methods

CM-SLP high-throughput screening

A375 and HaCaT cells were plated on 96-well plates at a density of 1×10^3 cells per well. After 24-hour incubation, the plates were washed three times with PBS (200 μL/well), and the cell culture medium was replaced with either high or low nutrient-containing medium. For the CM-SLP^{glu} platform, we used media containing 25 and 1 mmol/L glucose supplemented with normal FBS; for the CM-SLP^{gln} platform, we used media containing 2 and 0 mmol/L glutamine supplemented with normal FBS. For the CM-SLP^{FA} platform, we used normal versus charcoal-filtered fatty acid–depleted serum. The cells were then treated with an approved drug library (TargetMol) containing 1,813 compounds, each at 100 μmol/L. For each platform, cells were treated with drugs for 36 hours (CM-SLP^{glu}), 18 hours (CM-SLP^{gln}), and 60 hours (CM-SLP^{FA}), and then cell viability was measured with CellTiter 96 AQueous One Solution Assay (Promega), according to the manufacturer's instructions. Absorbance was then measured at 490 nm using the Infinite 200 PRO plate reader (Tecan Life Sciences). CM-SLP scores were calculated by following equation: CM-SLP score = $\log_{0.5}$ (cell viability at high nutrient/cell viability at low nutrient).

Cell culture

All cell lines were maintained at 37°C under 5% CO_2. The A375 (RRID: CVCL_0132), HaCaT (RRID: CVCL_0038), HEK293A (RRID: CVCL_6910), MEF (CVCL_4240), and Mel624 (RRID: CVCL_8054) cell lines were cultured in DMEM (Cytiva, SH30022.01) containing 10% FBS (HyClone, SV30207.02) and 50 μg/mL penicillin/streptomycin (Gibco, 15140122). 786-O (RRID: CVCL_1051), NCI-H1975 (RRID: CVCL_1511), NCI-H358 (RRID: CVCL_1559), BEAS-2B (RRID: CVCL_0168), BT549 (RRID: CVCL_1092), SNU886 (RRID: CVCL_5103), SNU878 (RRID: CVCL_5102), A549 (RRID: CVCL_0023), NCI-H1650 (RRID: CVCL_1483), NCI-H23 (RRID: CVCL_1483), 92.1 (RRID: CVCL_8607), y-Meso-26B (RRID: CVCL_5183), K562 (RRID: CVCL_0004), Molm14 (RRID: CVCL_7916), Nalm-6 (RRID: CVCL_0092), THP-1 (RRID: CVCL_0006), NCI-H69 (RRID: CVCL_8121), and NCI-H854 (RRID: CVCL_A584) cell lines were cultured in RPMI (HyClone, SH30027.01) containing 10% FBS (HyClone, SV30207.02) and 50 μg/mL penicillin/streptomycin (Gibco, 15140122). The HEMn and HEMa cell lines were cultured in Dermal Cell Basal Medium (ATCC, PCS-200-030) complemented with the Melanocyte Growth Kit (ATCC, PCS-200-041) and Adult Melanocyte Growth Kit (ATCC, PCS-200-042), respectively. The HREC cell line was cultured in Renal Epithelial Cell Basal Medium (ATCC, PCS-400-030) complemented with the Renal Epithelial Cell Growth Kit (ATCC, PCS-400-040). The MCF10A (RRID: CVCL_0598) cell line was cultured in DMEM-F12 (HyClone, SH30023.01) supplemented with 5% horse serum (Gibco, 16050122), 20 ng/mL EGF (PeproTech, 315-09), 0.5 μg/mL hydrocortisone (Sigma, H0135), 100 ng/mL cholera toxin (Sigma, SAE0069), and 10 μg/mL insulin (Sigma, I9278). Sk-mel-2 (RRID: CVCL_0069) and MRC-5 (RRID: CVCL_0440) cell lines were cultured in minimum essential medium (Cytiva, SH30024,01) containing 10% FBS (HyClone, SV30207.02) and 50 μg/mL penicillin/streptomycin (Gibco, 15140122). A375, HEK293A, 786-O, NCI-H1975, BEAS-2B, BT549, K562, Nalm-6, HEMn, HEMa, HREC, and MCF10A were purchased from ATCC. NCI-H358, SNU886, SNU878, A549, NCI-H1650, NCI-H23, THP-1, NCI-H69, NCI-H854, Sk-mel-2, and MRC5 cell lines were purchased from the Korean Cell Line Bank. HaCaT, Mel624, 92.1, y-Meso-26B, and Molm14 were kindly provided by K.-L. Guan. The p53 knockout (KO) and p53/TSC2 double-KO MEF cell lines were kindly provided by Y.-J. Jang. No cell lines used in this study were found in the database of commonly misidentified cell lines maintained by Internatinal Cell Line Authentication Commitee (ICLAC) and NCBI Biosample. To induce metabolic stress, cells were starved of glucose, glutamine, and fatty acids by switching them to glucose-free DMEM (Gibco, 1196025), glutamine-free DMEM (HyClone, SH30081.01), and charcoal-stripped FBS (Thermo Fisher Scientific, A3382101), respectively.

CRISPR KO cell lines

Glucose-6-phosphate isomerase (GPI)–, AMPKα1/2-, LATS1/2-, and LKB1-KO cell lines were engineered using the CRISPR/Cas9 gene-editing system. The guide RNA (gRNA) sequences targeting

these genes were designed using the CRISPR design tool available at http://www.rgenome.net/cas-designer/. The respective gRNA sequences employed were for GPI, #1 5′-GGTTCTTGGAGTAATCCACC-3′ and #2 5′-GCATCACGTCCTCCGTCACC-3′; for AMPKα1, #1 5′-GCGAGCTTCGTCCTCATGCAGGG-3′ and #2 5′-TACTCAATCGACAGAAGATT-3′; for AMPKα2, #1 5′-GAAGATCGGACACTACGTGC-3′ and #2 5′-CTACGTGCTGGGCGACACGC-3′; for LATS1, #1 5′-GCAGCCATCTGCTCTCGTCG-3′ and #2 5′-GGAGGTGGAGTTGTACCTCT-3′; for LATS2, #1 5′-GTAGGACGCAAACGAATCGC-3′ and #2 5′-TAGCCCCTGAACCGAAGACT-3′; and for LKB1, #1 5′-AGCTTGGCCCGCTTGCGGCG-3′ and #2 5′-CCACCGCATCGACTCCACCG-3′. The custom-designed gRNA sequences targeting GPI, AMPKα1, AMPKα2, LATS1, LATS2, and LKB1 were cloned into the px459 vector (Addgene, plasmid no. 62988). Following DNA sequencing to verify the accuracy of the insertions, the plasmids containing the desired sequences were transferred to DH5α *Escherichia coli* to complete cloning. The cloned px459 vectors were then transfected into HEK293A cells. After transfection, the cells were subjected to puromycin selection. Individual HEK293A clones were separated into 96-well plates using a BD FACSAria III cell sorter (BD Biosciences). The successful generation of KO clones was subsequently confirmed through Western blot analysis.

Chemical agents

Propafenone hydrochloride (P4670), metformin hydrochloride (#PHR1084), warfarin (#A2250), fenbendazole (#PHR1832), phenformin hydrochloride (#PHR1573), fructose (#F3510), oligomycin A (#75351), and BAY-876 (SML1774) were purchased from Sigma-Aldrich. Verapamil hydrochloride (#14288), paxilline (#11354), flecainide acetate (#20388), procainamide hydrochloride (#24359), quinidine (#20356), lidocaine (#20081), phenytoin (#24037), sotalol hydrochloride (#16136), diltiazem hydrochloride (#20079), nilutamide (#23953), cisapride (#21657), dabrafenib (#16989), trametinib (#16292), and valdecoxib (#10006120) were purchased from Cayman Chemical. Tram-34 (S1160), tetraethylammonium (TEA) chloride (S4489), propranolol hydrochloride (S4076), metoprolol (S5430), and temsirolimus (S1044) were purchased from Selleckchem. Rapalink-1 (A8764) was purchased from Biotrend.

Immunofluorescence microscopy

Cells were seeded onto 12-well plates on coverslips 1 day prior to experimentation. Coverslips were pretreated with poly-L-ornithine solution (Sigma, P4957) diluted 1:20 at 37°C for 15 minutes, followed by a quick PBS wash prior to cell seeding. The cells were then fixed in 4% paraformaldehyde (Thermo Fisher Scientific, 28908) for 20 minutes and permeabilized in 0.1% Triton-X/PBS for 5 minutes. The cells were blocked in 3% BSA/PBS for 30 minutes and incubated overnight at 4°C in primary antibodies diluted in 3% BSA/PBS. Then the cells were incubated for 2 hours in secondary antibodies diluted in 3% BSA/PBS. The slides were mounted in ProLong Gold Antifade reagent with DAPI (Invitrogen, P36930). Single Z section images at the same cellular level were captured with a confocal microscope (Leica Microsystems, SP8). The images depicted in the figures were processed and exported using ImageJ.

Immunoprecipitation and immunoblotting

Immunoblotting was performed using a standard protocol. Phos-tag reagents were purchased from Wako Chemicals, and gels containing phos-tag were prepared according to the manufacturer's instructions. For immunoprecipitations, cells were rinsed twice with ice-cold PBS and lysed in ice-cold lysis buffer [0.15 mol/L NaCl, 0.05 mol/L Tris-HCl, 0.5% Triton X-100, and one tablet each of EDTA-free protease and phosphatase inhibitors (Thermo Fisher Scientific, 78446)]. For immunoprecipitations, anti-Myc magnetic beads (Thermo Fisher Scientific, 88842) were added to the lysates and incubated with rotation overnight at 4°C. The resulting immunoprecipitates were washed three times with lysis buffer. The immunoprecipitated proteins were then denatured with the addition of sample buffer and subjected to boiling for 7 minutes. Then, they were resolved via 8% SDS-PAGE and analyzed via Western blotting.

Antibodies

The following antibodies were purchased from Cell Signaling Technology and used at the indicated dilutions for Western blot analysis, IHC, and immunofluorescence: pS6K (#9234, RRID: AB_2269803), S6K (#2708, RRID: AB_390722), pAKT (#4060, RRID: AB_2315049), AKT (#4685, RRID: AB_2225340), pAMPK (#2535, RRID: AB_331250), AMPK (#2603, RRID: AB_490795), pACC (#11818, RRID: AB_2687505), ACC (#3676, RRID: AB_2219397), YAP (#14074, RRID: AB_2650491), TAZ (#4883, RRID: AB_1904158), LATS (#9153, RRID: AB_2296754), pan-TEAD (#13295, RRID: AB_2687902), p-p38 MAPK (#4511, RRID: AB_2139682), p38 MAPK (#8690, RRID: AB_10999090), pERK 1/2 (#4377, RRID: AB_331775), ERK 1/2 (#4695, RRID: AB_390779), pFAK (#3283, RRID: AB_2173659), FAK (#3285, RRID: AB_2269034), pLATS (#8654, RRID: AB_10971635), LATS (#3477, RRID: AB_2133513), and IgG (#2729, RRID: AB_1031062). The following antibodies was purchased from Santa Cruz Biotechnology and used at the indicated dilutions for Western blot analysis and immunofluorescence: Myc-HRP (sc-40, RRID: AB_627268), GAPDH (#sc-25778, RRID: AB_10167668), and vinculin (#sc-73614, RRID: AB_1131294). Paxillin (#610569, RRID: AB_397918) antibody was purchased from BD Biosciences. Rhodamine-Phalloidin (#R415) was purchased from Thermo Fisher Scientific. The following antibodies were purchased from Abcam and used at the indicated dilutions for Western blot analysis: GLUT5 (ab279363, RRID: AB_3712112) and GLUT2 (ab192599, RRID: AB_3712113).

Extracellular flux analysis

786-O renal cancer cells (3×10^3) were distributed into the individual wells of 96-well plates (Agilent Technologies, 103774-100), with six wells designated for each experimental group. To serve as a negative control, the four corners of the plate were deliberately left empty of cells. In these regions, only Seahorse media were provided. After 24 hours of incubation, each well was washed with 100 μL of PBS and then the cells were resuspended in prewarmed (37°C) DMEM with either 25 mmol/L glucose or 0.5 mmol/L glucose, 40 μmol/L propafenone, or 30 μmol/L paxilline and DMSO for each control group. After 24 hours of pretreatment, the 786-O cells were washed with PBS and then resuspended in Seahorse Basal Medium supplemented with 2 mmol/L glutamine and either 25 mmol/L glucose or 0.5 mmol/L glucose at pH 7.4 for ATP Real-Time Assays.

Using a Seahorse XF96 Analyzer (Agilent Technologies), we measured extracellular acidification rate (ECAR) and oxygen consumption rate (OCR) in accordance with the manufacturer's instructions. Baseline OCR and ECAR values were obtained through three initial measurements, followed by the injection of Seahorse XF Real-Time ATP Rate Assay Kit reagents. The final concentrations of these reagents (1.5 μmol/L oligomycin-A, 0.5 μmol/L rotenone, and 0.5 μmol/L antimycin A) were achieved using the Seahorse XF

Real-Time ATP Rate Assay Kit (#103592-100) from Agilent. Subsequent measurements were facilitated by the ATP Real-Time Rate Assay Generator (Agilent Technologies). Afterward, 786-O cells were normalized to the protein concentration per well as measured via a Bradford assay kit (#5000006) purchased from Bio-Rad.

The real-time analysis of ATP production was conducted using the Seahorse XFp Analyzer (Agilent Technologies) and the Seahorse XFp Real-Time ATP Rate Assay Kit (Agilent Technologies, 103591-100) according to the manufacturer's guidelines. A375 cells were seeded into XFp cell culture miniplates (Agilent Technologies, 103025-100) at a density of 1×10^4 cells per well. After 24 hours of incubation, each well was washed with 100 μL of PBS. Then, the medium was replaced with either 25 mmol/L or 0 mmol/L glucose-containing medium. Three hours after this medium change, 25 mmol/L metformin was added and incubated for 8 hours. After this drug incubation period, each miniplate was placed in the XFp analyzer along with the XFp sensor cartridge that contained the drug from the assay kit to measure real-time ATP production. These analyses were conducted according to the manufacturer's instructions.

ATP assay

ATP levels were measured to determine whether the reduction in ATP production induced by combined treatment with glucose restriction and metformin could be rescued by fructose. A375 cells were seeded into 12-well plates at 5×10^5 cells per well. After 24-hour incubation, the cells were washed twice with PBS. Then, the medium was replaced with medium containing either 25 mmol/L or 0 mmol/L glucose. Three hours after the medium change, 10 mmol/L metformin was added and incubated for 8 hours. ATP levels were then measured with the ATP Detection Assay Kit (Cayman Chemical, 700410) according to the manufacturer's instructions.

Cell viability assay

Cell viability assays were conducted to determine whether the cell death effect of combined treatment with glucose restriction and metformin is rescuable by fructose. A375 cells were seeded into 12-well plates at 5×10^5 cells per well. After 24-hour incubation, the cells were washed twice with PBS and then the medium was replaced with medium containing either 25 mmol/L or 0 mmol/L glucose. Three hours after the medium change, 10 mmol/L metformin was added and allowed to incubate for 16 hours. Subsequently, photographs of the cells were taken. After a single PBS wash, the medium was replaced with DMEM containing MTT at a 1:100 dilution from a 12 mmol/L stock solution (Thermo Fisher Scientific, M6494). Four hours after the medium change, the medium was removed, and the cells were solubilized with 300 μL of DMSO to measure absorbance and analyze cell viability. As MTT reduction is dependent on cellular metabolic activity, changes in metabolic states could influence the results. Therefore, we also confirmed cellular morphology via microscopy to support MTT-based viability results. In **Fig. 7A**, each data point in the graph was calculated using a two-step normalization process. First, relative cell viability for each cycle was calculated as relative cell viability = (cell viability of glucose + metformin group)/(cell viability of glucose control group at the same time point) × 100. Next, these values were normalized to cycle 0 as normalized relative cell viability = (relative cell viability at cycle X)/(relative cell viability at cycle 0) × 100.

RNA extraction, cDNA synthesis, and qRT-PCR

Cells were harvested for RNA extraction using the RNeasy Plus Mini kit (Qiagen, 74136). RNA samples were reverse transcribed to cDNA using iScript Reverse Transcriptase (Bio-Rad, 1708891). qRT-PCR was performed using the KAPA SYBR FAST qPCR kit (Kapa Biosystems, KK4605) and the StepOnePlus Real-Time PCR System (Applied Biosystems). The qRT-PCR primers were as follows: for CTGF, forward, 5′- ATGACACTGTTCAGGAATCG 3′ and reverse, 5′- CAAATTCACTTGCCACAAGC; for ANKRD1, forward, 5′- CACTTCTAGCCCACCCTGTGA -3′ and reverse, 5′- CCACAGGTTCCGTAATGATTT -3′; and for GAPDH, forward, 5′- ACCAGGTGGTCTCCTTCGAC -3′ and reverse, 5′- TGCT GTAGCCAAATTCGT -3′.

Animal experiments

NOD/SCID mice were purchased from JaBio. For the tumor xenograft models, 786-O renal cancer cells (5×10^6) were injected subcutaneously into the right flank of 6-week-old male nude mice. Seven days after the injections, the mice were assigned randomly to treatment groups, eight mice per group. For *in vivo* drug treatments, NOD/SCID mice were given intraperitoneal injections 4 days a week with propafenone (30 mg/kg), temsirolimus (0.3 mg/kg), propafenone (30 mg/kg) with temsirolimus (0.3 mg/kg), Bay-876 (5 mg/kg), propafenone with Bay-876 (5 mg/kg), or vehicle (PBS). Propafenone, temsirolimus, and Bay-876 were diluted in PBS and thoroughly sonicated. Mouse weights were measured every week. Tumor weight and volume were measured after the animals were sacrificed. Mice were sacrificed 6 weeks after the experiment began. BALB/C nude mice were purchased from JaBio. For the tumor xenograft models, A375 melanoma cells (2×10^5) and NCI-H1975 lung cancer cells (5×10^5) were injected subcutaneously into the right flank of 6-week-old male nude mice. When the resulting tumors reached a size of 100 mm^2, the mice were assigned randomly to treatment groups. The investigators were not blind to these allocations during the experiments or the outcome assessments. To manipulate mouse blood glucose, mice in the carbohydrate-free group were fed carbohydrate-free chow according to the average weight of AIN-93M control chow. For *in vivo* metformin treatments, nude mice were given daily intraperitoneal injections of metformin diluted in PBS at doses of 200 mg/kg. Tumor volume and mouse weight were measured every week (volume = width × width × height/2) and blood glucose was measured daily with a blood glucose monitor (Glucodoctor). The mice were euthanized 6 weeks after tumor engraftment. K-Ras-LA2 mice were purchased from The Jackson Laboratory. These mice were bred in a specific pathogen-free (SPF) facility in the Yonsei Laboratory Animal Research Center. *In vitro* fertilization was used to augment the cancer model mice. They were fed a normal chow diet (PicoLab Rodent Diet 20, Orient Bio, Inc.) and maintained under a 12-hour light–dark cycle in the SPF facility at 23°C and 40% to 60% humidity. For the *in vivo* BMY-123 and metformin treatments, LA2 mice were given daily intraperitoneal injections with 10 mg/kg of BMY-123 and 200 mg/kg metformin. BMY-123 was diluted in PBS and thoroughly sonicated. Mice were sacrificed 10 weeks after the experiment began. All animal experiments were approved by the Yonsei University Institutional Animal Care and Use Committee (documentation #201610-435-02).

Patch clamp solutions

Whole-cell voltage clamp experiments were conducted using a basal extracellular solution containing 130 mmol/L NaCl, 4 mmol/L

KCl, 10 mmol/L HEPES, 10 mmol/L glucose, 1 mmol/L $CaCl_2$, and 1 mmol/L $MgCl_2$, with its pH adjusted to 7.4 using NaOH and its osmolarity adjusted to ~310 mOsM with an appropriate amount of sorbitol. The basal pipette solution with 1 μmol/L free Ca^{2+} contained 130 mmol/L KCl, 10 mmol/L HEPES, 5 mmol/L EGTA, 4.37 mmol/L $CaCl_2$, and 3 mmol/L Mg-ATP, with its pH adjusted to 7.2 using KOH and its osmolarity adjusted to ~290 mOsM with an appropriate amount of sorbitol. Free Ca^{2+} was calculated using the WEBMAX-C software (C. Patton, Stanford University; https://somapp.ucdmc.ucdavis.edu/pharmacology/bers/maxchelator/webmaxc/webmaxcS.htm). The pipette solution with zero free Ca^{2+} was made by omitting $CaCl_2$.

For measuring current–voltage relationships, currents were evoked with a 50-millisecond prepulse at −90 mV prepulse for 50 milliseconds, then −90 to 100 mV test pulses for 200 milliseconds with 10-mV increments, and −90 mV postpulse for 50 milliseconds. Channel activity was calculated as the average current density during the last 50 milliseconds of each test pulse. To access drug inhibition, currents were evoked by −90 mV prepulse for 50 milliseconds, then 100 mV test pulses for 200 milliseconds, and then −90 mV postpulse for 50 milliseconds. Channel activity was calculated as the average current density during the last 50 milliseconds of the test pulse.

For recording voltage-activated Na^+ currents, the extracellular solution contained 130 mmol/L NaCl, 4 mmol/L CsCl, 1 mmol/L $MgCl_2$, 10 mmol/L glucose, 10 mmol/L HEPES, and 100 μmol/L $CdCl_2$, with its pH adjusted to 7.4 using NaOH and its osmolarity adjusted to ~310 mOsM with sorbitol. The intracellular solution contained 117 mmol/L CsCl, 20 mmol/L NaCl, 1 mmol/L $MgCl_2$, 5 mmol/L HEPES, and 5 mmol/L EGTA, with its pH adjusted to 7.2 using KOH and its osmolarity adjusted to ~290 mOsM with sorbitol.

For recording voltage-activated Ca^{2+} currents, the extracellular solution contained 120 mmol/L NaCl, 5 mmol/L CsCl, 0.5 mmol/L $MgCl_2$, 10 mmol/L $BaCl_2$, 10 mmol/L HEPES, 10 mmol/L TEA-Cl, and 10 mmol/L glucose, with its pH adjusted to 7.4 using NaOH and its osmolarity adjusted to ~300 mOsM with sorbitol. The intracellular solution contained 100 mmol/L CsOH, 100 mmol/L aspartic acid, 32 mmol/L CsCl, 10 mmol/L EGTA, 10 mmol/L HEPES, and 5 mmol/L Mg-ATP, with its pH adjusted to 7.2 using CsOH and its osmolarity adjusted to ~290 mOsM using sorbitol.

Electrophysiology

Cells were transferred to a bath perfused at 5 mL/minute and mounted on the stage of an inverted microscope (Nikon). Microglass pipettes (World Precision Instruments) were fabricated using a PP-830 single-stage glass microelectrode puller (Narishige), with a resistance of 2 to 5 MΩ. The liquid junction potential was rectified using an offset circuit prior to each recording. Currents were recorded using an Axopatch 200B amplifier (Molecular Devices) and Digidata 1440A interface (Molecular Devices), digitized at 20 kHz and low-pass filtered at 2 kHz using pClamp software 10.7 (Molecular Devices). All recordings were performed at room temperature (22°C–25°C). The whole-cell voltage clamp configuration was verified by measuring the series resistance to <10 MΩ, which was compensated before each recording.

In the whole-cell configuration, K^+ currents were recorded at a holding potential of –60 mV, and chemicals were applied after >5 minutes of break-in to reduce the effects of channel activation. The chemicals were tested for >5 minutes to obtain a stable current level. To measure the channel activity on blocker administration experiments, cells were held at currents, which were evoked by −90 mV prepulse for 50 milliseconds, then −90 to 100 mV test pulses for 200 milliseconds with 10 mV increment, and then −90 mV postpulse for 50 milliseconds. Channel activity was calculated as the average current density in the last 50 milliseconds of each test pulse. All experiments were performed in independent biological replicates, and the mounting chamber was replaced with new cells after each chemical.

Protein structure preparation

The X-ray crystal structure of human YAP bound to TEAD1 was retrieved from the Protein Data Bank (PDB ID: 3KYS). All the missing side chains were filled in using Prime (RRID: SCR_014887) implemented in Maestro program (9). Hydrogen atoms were added to the crystal structure at pH 7.0 and their positions were optimized with PROPKA implemented in Maestro program (10). Then the restrained energy minimizations were performed with an OPLS3 force field set to 0.3 Å root mean square deviation (11).

Virtual screening

To find compounds that inhibit the protein–protein interaction (PPI) between TEAD1 and YAP, pharmacophore-based virtual screening was performed on our in-house synthetic database using Phase (RRID: SCR_014884) implemented in the Schrödinger suite (RRID: SCR_016748; refs. 12, 13). Pharmacophores were generated for the PPI between TEAD1 and YAP. The top-hit inhibitor, BMY-123, was selected from the pharmacophore-based screening. Then molecular docking was performed using Glide (RRID: SCR_000187) implemented in the Schrödinger suite (14). The docking position of BMY-123 bound to TEAD1 was selected using its glide score, e-model score, and by visual inspection.

Fragment molecular orbitals

To analyze the interactions between TEAD1 and BMY-123 at the molecular level, we performed an *ab initio* fragment molecular orbital (FMO) analysis. All FMO calculations were performed using GAMESS (RRID: SCR_014896; ref. 15). The energy minimization of the top-hit docking pose of BMY123 was performed at FMO-DFTB3/D/PCM level with the third order corrected density functional tight-binding (DFTB3) method using the 3OB parameter set (16, 17), UFF-type dispersion correction (D; ref. 18), and polarizable continuum model (PCM; ref. 19). In energy minimization, the residues within 10.4 Å from the ligand were 908 included and fixed, and only the ligand was allowed to remain fully flexible. The energy minimization calculations converged in 61 steps.

An energy decomposition analysis was performed with the energy minimized structure at the FMO-MP2/PCM level with the second order Møller–Plesset perturbation theory (MP2; ref. 20) and a PCM (21) using the 6-31G** basis set. All the residues in the crystal structure were included in the energy decomposition analysis. The binding affinity of the protein–ligand interaction was approximated as the sum of their pair interaction energies (PIE). Each PIE provided physical details of the protein–ligand interactions (22, 23). The PIEs between fragments in the FMO calculations were decomposed by five energy terms defined by Eq. A: electrostatic (ΔE^{es}), exchange-repulsion (ΔE^{ex}), charge transfer with a higher order mixed term (ΔE^{ct+mix}), dispersion (ΔE^{di}), and solvation energy (ΔG_{sol}) from the PCM.

$$\Delta E^{int} = \Delta E^{es} + \Delta E^{e}\mathrm{x} + \Delta E^{ct+mix} + \Delta E^{di} + \Delta G_{sol} \qquad \text{A}$$

The electrostatic term is mainly derived from the Coulomb interaction between the polarized charge distributions of the

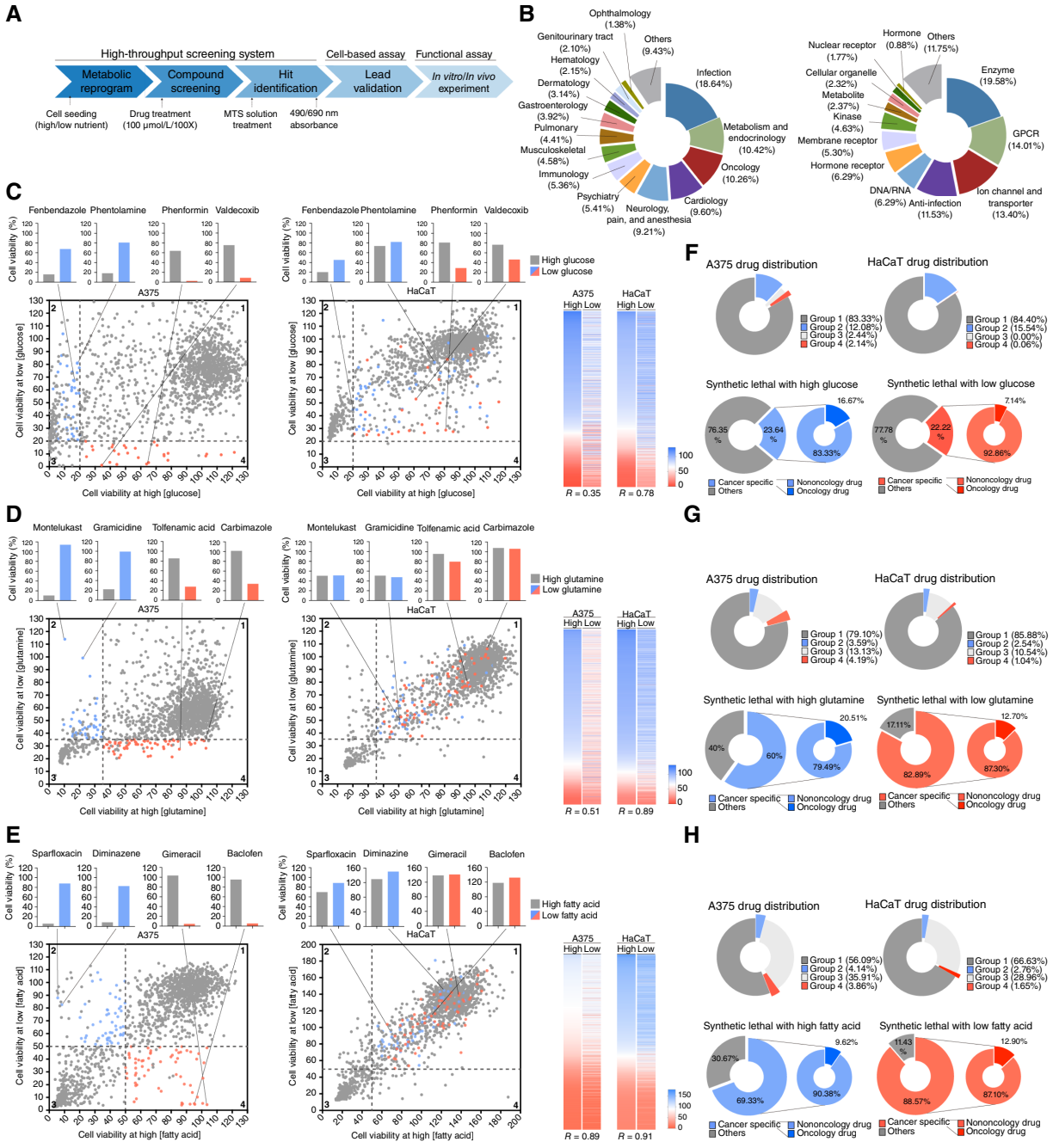

Figure 1.

Landscape of the metabolic vulnerabilities of nononcology drugs according to nutrient availability. **A,** Schematic overview of the high-throughput CM-SLP screening system. A toal of 1,813 bioactive compounds were added to A375 melanoma and HaCaT keratinocyte cells under high- or low-nutrient concentrations, and cell viability was measured for each drug/nutrient status combination. **B,** Composition of the CM-SLP drug library sorted by drug indications (left) and drug targets (right). **C–E,** Dot plot summarizing the screen results from CM-SLP^{glu}, CM-SLP^{gln}, and CM-SLP^{FA} performed with the A375 (left) and HaCaT (right) cell lines. *X*-axis, relative cell viability at high nutrient concentrations; *y*-axis, relative cell viability at low nutrient concentrations. The dot plots are divided into four quadrants (group 1, top right; group 2, top left; group 3, bottom left; group 4, bottom right) that distinguish drugs according to their cancer cell specificity. Blue dots, cancer cell–specific group 2 drugs; red dots, cancer cell–specific group 4 drugs. The bar graphs above the panels show cell viabilities of representative group 2 and group 4 candidate drugs. Left, *y*-axis, relative cell viability at high/low nutrient concentrations. Right, heatmap of CM-SLP and the correlation coefficient values (*R*) for each platform performed with A375 and HaCaT cells. **F–H,** Analysis of CM-SLP candidates from CM-SLP^{glu}, CM-SLP^{gln}, and CM-SLP^{FA} performed with A375 and HaCaT cells. Drug composition of the CM-SLP results by quadrant (top row). The percentages of cancer-specific cytotoxic drugs in groups 2 and 4, as well as the percentage of nononcology vs. oncology drugs among the cancer-specific drugs, are shown for each CM-SLP screen performed with A375 cells (bottom row).

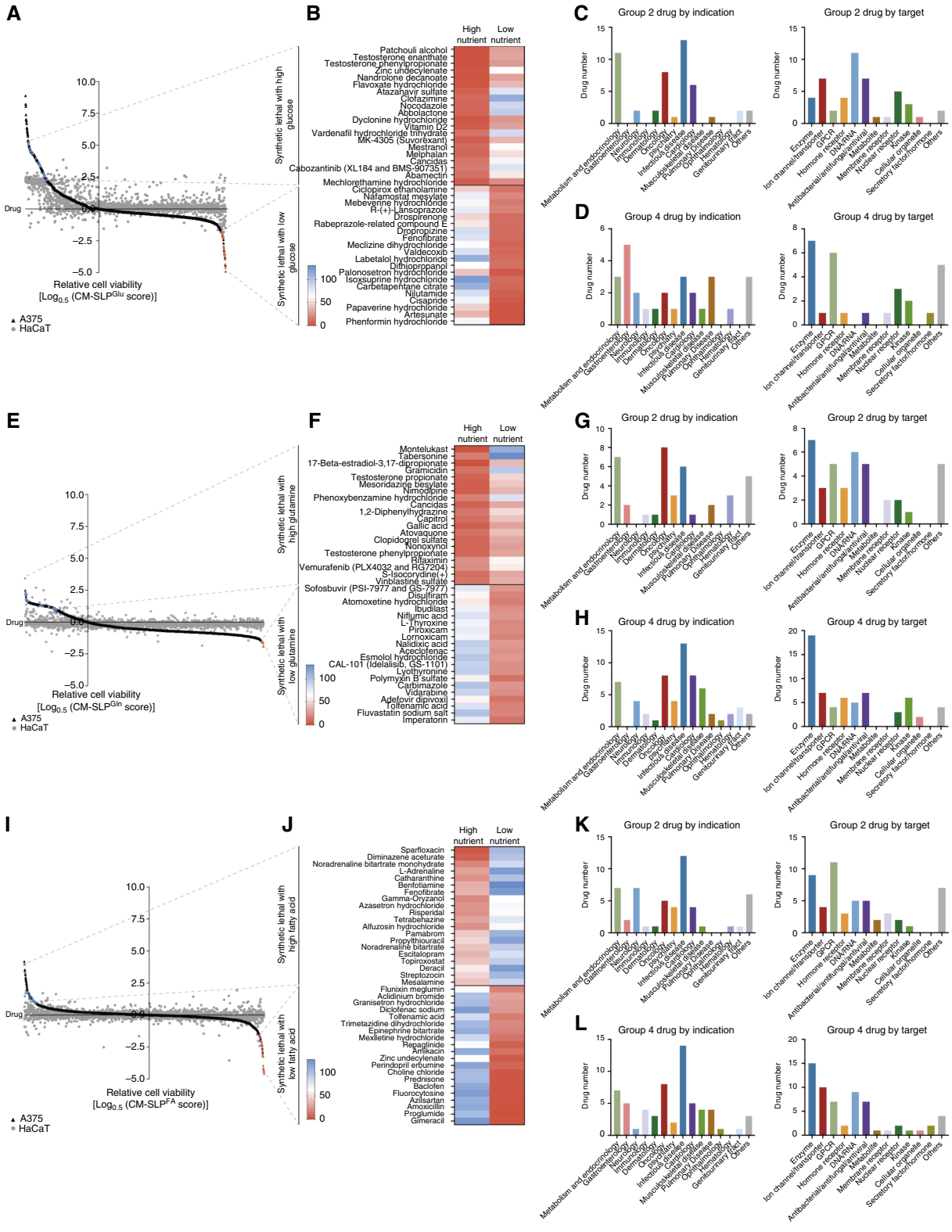

Figure 2.

Nutrient availability–dependent anticancer drug repurposing opportunities. **A,** High-throughput screening results for the CM-SLP^{glu} panels. Drugs are listed according to their individual top CM-SLP scores (left). **B,** Heatmap of top CM-SLP candidates that show significant CM-SLP scores from groups 2 and 4 of the CM-SLP^{glu} screens (min, 0; max, 130). **C** and **D,** Indications and molecular target analyses of group 2 and 4 CM-SLP (*Continued on the following page.*)

fragments. The charge transfer term is derived from the interaction between the occupied orbitals of a donor and the unoccupied orbitals of an acceptor. The electrostatic and charge transfer terms are important for assigning hydrogen bond, salt bridge, and polar interaction positions. The exchange-repulsion term is derived from the interactions between fragments located in proximity with one another. The dispersion term derived from the interaction of the induced dipole moments of two fragments. The exchange-repulsion term describes steric repulsion, whereas the dispersion term represents hydrophobic in nature.

Surface plasmon resonance assay

Surface plasmon resonance (SPR) analysis was used to investigate whether BMY-123 binds to TEAD1. Upon injection of BMY-123 over the sensor surface immobilized with TEAD1, changes in refractive index and mass concentration were observed. To assess the binding selectivity of BMY-123 compounds toward TEAD1, SPR measurements were conducted to analyze the interaction between TEAD1 and BMY-123.

A full-length TEAD1 protein containing a His-tag was purified and supplied by Young Frontier Co., Ltd. The interaction studies between BY03 and TEAD1 were carried out using the ProteOn XPR36 Protein Interaction Array System (Bio-Rad). TEAD1 was immobilized onto a ProteOn GLH sensor chip via amine coupling. The ligand solutions were prepared in 1× PBS supplemented with Tween 20% and 1% DMSO at varying concentrations (0, 6.25, 12.5, 25, and 50 μmol/L) and injected over the sensor chip at a flow rate of 100 μL/minute.

Binding kinetics were analyzed using ProteOn Manager Software 2.0 (Bio-Rad). Kinetic data were fitted to standard Langmuir binding models. The association rate constant (k_a; M/s) reflected the rate at which the complex formed, whereas the dissociation rate constant (k_d in s^{-1}) indicated the rate of complex dissociation. High-affinity interactions were characterized by low K_D values, whereas rapid recognition and binding of the interactants (rapid "on rate" or high k_a) and stability of the complex formed (slow "off rate" or low k_d) were represented by the equation $K_D = k_d/k_a$.

Statistics and reproducibility

All quantitative data were obtained from at least three independent biological replicates. All data are presented as means ± SD unless otherwise noted in the figure legends. Statistical differences between two groups were examined using two-tailed, unpaired Student *t* tests or one-way ANOVA with Bonferroni corrections for multiple comparisons. Statistical tests were performed using the GraphPad Prism 9.0 software (GraphPad Software). Two-sided *P* values of less than 0.05 were considered significant. No statistical methods were used to predetermine sample size. Sample size was based on previous experience with experimental variability. Blinding was performed wherever possible during all sample analyses by coding sample identity during data collection and having the following analyses performed by observers without knowledge of or access to the experimental conditions.

Results

Metabolic vulnerability landscape for nononcology drugs according to nutrient availability

A panel of bioactive compounds, mostly FDA-approved drugs, was analyzed using CM-SLP to identify synthetic lethality between commonly prescribed medications and specific metabolite concentrations, offering a resource to prioritize clinically relevant drug–metabolite interactions. A total of 1,813 FDA-approved compounds were screened for metabolite-dependent cytotoxicity in A375 melanoma cells and HaCaT keratinocytes as normal counterpart (**Fig. 1A** and **B**), using media with high versus low concentrations of glucose, glutamine, or fatty acids. For CM-SLP^{glu}, 25 and 1 mmol/L glucose was used (**Fig. 1C**); for CM-SLP^{gln}, 2 and 0 mmol/L glutamine was used (**Fig. 1D**); and for CM-SLP^{FA} platform, normal versus charcoal-filtered serum, which has lowered lipid content, was used (**Fig. 1E**). Culture media were adapted from standard formulations, modified with nutrient-depleted conditions.

Four quadrants based on correlation coefficients (r) were applied to assess differential cytotoxicity and cancer cell specificity. Notably, lower correlation coefficients in cancer cells indicate that their metabolic rewiring renders them more vulnerable to various drugs compared with normal cells. Drugs in the first (group 1, top right) and third quadrants (group 3, bottom left) demonstrate minimal and maximal cytotoxicity, respectively, regardless of metabolite concentration. In contrast, the second (group 2, top left) and fourth quadrants (group 4, bottom right) contained compounds exhibiting metabolite concentration–dependent synthetic lethality, highlighting the significant influence of nutrient availability on the cytotoxicity of these drugs (**Fig. 1C–E**).

We identified compounds for which cytotoxicity was selectively altered by nutrient availability, specifically glucose (group 2, 12.08%; group 4, 2.14%), glutamine (group 2, 3.59%; group 4, 4.19%), and fatty acid (group 2, 4.14%; group 4, 3.86%). Among these drugs, essential subsets elicited cancer cell–specific cytotoxicity, including glucose (group 2, 23.64%; group 4, 22.22%), glutamine (group 2, 60%; group 4, 82.89%), and fatty acid (group 2, 69.33%; group 4, 88.57%; **Fig. 1F–H**). To our surprise, many compounds in groups 2 and 4 that elicited both metabolite-dependent and cancer cell–specific synthetic lethality were nononcology drugs, suggesting the potential of CM-SLP to identify metabolite-dependent repurposing opportunities for a broad spectrum of nononcology drugs. Representative compounds are shown above each CM-SLP panel (**Fig. 1C–E**). CM-SLP^{glu} revealed 48 compounds with cancer cell–specific synthetic lethality in high-glucose (e.g., fenbendazole and phentolamine) and 28 low-glucose hits (e.g., phenformin and valdecoxib; **Fig. 1C**). CM-SLP^{gln} identified 39 high-glutamine (e.g., montelukast and gramicidin) and 63 low-glutamine hits (e.g., tolfenamic acid and carbimazole; **Fig. 1D**). CM-SLP^{FA} found 52 high–

(*Continued*.) candidates from the CM-SLP^{glu} screens. **E,** High-throughput screening results for the CM-SLP^{gln} panels. Drugs are listed according to their individual top CM-SLP scores (left). **F,** Heatmap of top CM-SLP candidates that show significant CM-SLP scores from groups 2 and 4 of the CM-SLP^{gln} screens (min, 0; max, 130). **G** and **H,** Indications and molecular target analyses of group 2 and 4 CM-SLP candidates from the CM-SLP^{gln} screens. **I,** High-throughput screening results for the CM-SLP^{FA} panels. Drugs are listed according to their individual top CM-SLP scores (left). **J,** Heatmap of top CM-SLP candidates that show significant CM-SLP scores from groups 2 and 4 of the CM-SLP^{FA} screens (min, 0; max, 130). **K** and **L,** Indications and molecular target analyses of group 2 and 4 CM-SLP candidates from the CM-SLP^{FA} screens. **A**, **E**, and **I,** *X*-axis, dot plot of individual compounds; *y*-axis, CM-SLP scores; blue dots, cancer cell–specific group 2 drugs; red dots, cancer cell–specific group 4 drugs; black dots, CM-SLP results performed with A375 cells; gray dots, CM-SLP results performed with HaCaT cells.

fatty acid (e.g., sparfloxacin and diminazene) and 62 low–fatty acid hits (e.g., gimeracil and baclofen; **Fig. 1E**). These results demonstrate how nutrient availability influences nononcology drug response and provide insights to design metabolically informed synthetic lethal combination therapies.

Nutrient availability–dependent anticancer drug repurposing opportunities

The CM-SLP score represents the ratio between cell viability in the context of high versus low metabolite concentrations. CM-SLP scores were calculated by the following equation: CM-SLP score = $\log_{0.5}$ [(cell viability at high nutrient)/(cell viability at low nutrient); Supplementary Tables S1–S3]. Compounds with significantly high or low CM-SLP scores were considered nutrient-sensitive and cancer-specific hits. CM-SLP^{glu} yielded the lowest *R* value and drugs with most significant CM-SLP score (**Fig. 2A** and **B**). Notably, although nutrient deprivation typically increases cytotoxicity, group 2 drugs in CM-SLP^{glu}, commonly used in infectious diseases, endocrinology, and oncology, exhibited enhanced cytotoxicity under hyperglycemia (**Fig. 2C**; ref. 1). Given that hyperglycemia is both a side effect of anticancer therapies and a risk factor for cancer progression (24, 25), these drugs may benefit patients with comorbid metabolic syndromes such as diabetes, insulin resistance, or obesity.

Conversely, group 4 CM-SLP^{glu} drugs, including those used in gastroenterology, endocrinology, and pulmonology, exhibited enhanced efficacy under hypoglycemia (**Fig. 2D**). This effect aligns with clinical strategies like caloric restriction or intermittent fasting (IF), which can potentiate therapy by exploiting metabolic vulnerabilities of cancer versus normal cells (4, 7, 26). Synergistic effects might also be achieved by combining these drugs with glucose-lowering agents such as GLUT, SGLT2 inhibitors, or GLP-1 agonists. Mechanistically, many group 4 drugs, such as phenformin, nilutamide, and valdecoxib, target mitochondrial function, implicating disruption of metabolic shift between glycolysis/oxidative phosphorylation (OXPHOS) as a key vulnerability (27–29).

In CM-SLP^{gln}, group 2 and group 4 drugs with significant CM-SLP scores spanned diverse therapeutic classes, including oncology, endocrinology, cardiology, and infectious diseases (**Fig. 2E–H**). These compounds target enzymes, GPCRs, DNA/RNA, and pathogens, underscoring the repurposing potential across diverse indications (**Fig. 2G** and **H**).

In CM-SLP^{FA}, group 2 drugs prescribed in infectious, endocrine, and neurologic disorders often induced DNA damage, potentially exploiting the elevated DNA replication stress in cancer cells (**Fig. 2I–K**; refs. 30–32). As with glucose, excess fatty acids promote proliferative signaling, and hyperlipidemia is a known cancer risk factor (24, 33), reinforcing the clinical relevance of these agents. Group 4 drugs in CM-SLP^{FA}, including those used in oncology and metabolic diseases, target enzymes, channels, and transporters, offering broad mechanistic potential in low-lipid conditions (**Fig. 2L**).

Collectively, these findings identify top CM-SLP drugs that are nutrient-sensitive, cancer-selective, and metabolite-guided repurposing candidates. Group 2 drugs may be suited for patients with hypermetabolic cancer, whereas group 4 agents could complement dietary or metabolic interventions, providing a tailored approach to enhance therapeutic outcomes.

Nutrient-sensitive cytotoxicity driven via cancer-related signaling perturbations

As the CM-SLP^{glu} screen yielded the lowest *R* value, indicating glucose as the most impactful metabolite on drug sensitivity, we validated candidate drugs from this screen based on their CM-SLP scores and cancer cell specificity. To mimic glucose fluctuations, we used high (25 mmol/L)- and low (1 mmol/L)-glucose conditions, as well as a GLUT inhibitor. As anticipated, warfarin (group 1) showed no cytotoxicity across glucose conditions (**Fig. 3A**). In contrast, fenbendazole (group 2) demonstrated cytotoxicity under high glucose but not in glucose-restricted conditions (**Fig. 3B**). Group 4 drugs, phenformin, valdecoxib, verapamil, and nilutamide, were minimally cytotoxic in high glucose but synergistically lethal under low glucose or GLUT inhibition (**Fig. 3C–F**), confirming that nutrient availability critically influences drug efficacy.

To assess clinical relevance, we tested a range of physiologically plausible glucose levels feasible to achieve in human patients. Normal glucose level was set to 5 mmol/L, hypoglycemia to <5 mmol/L, and hyperglycemia to >5 mmol/L. Remarkably, glucose level below 5 mmol/L was sufficient to trigger propafenone and phenformin cytotoxicity, whereas glucose level above 5 mmol/L induced fenbendazole cytotoxicity (**Fig. 3G** and **H**). These results align with pathophysiologic glucose ranges in patients with cancer, underscoring potential translational value (26).

Next, we examined cancer-related signaling pathways affected by glucose fluctuations. Consistently, warfarin (group 1) did not affect AMPK, Hippo, MAPK, or mTOR signaling under both high- and low-glucose concentrations (**Fig. 3I**). However, fenbendazole (group 2) altered YAP/TAZ and p38 signaling under high glucose (**Fig. 3J**), and group 4 drugs, phenformin, valdecoxib, verapamil, and nilutamide, altered AMPK, mTOR, p38, YAP/TAZ, and ERK signaling under low glucose (**Fig. 3K–N**). As these compounds are known to induce mitochondrial dysfunction, the synergism with hypoglycemic conditions may arise from impaired energy sensing and signaling pathways.

To extend these findings, we compared nononcology CM-SLP^{glu} candidates with oncology drugs. We selected fenbendazole (group 2) and phenformin (group 4) for comparison with melanoma- and non–small cell lung cancer–targeted therapies. Oncology drugs within the FDA-approved drug panel were distributed across groups 1 through 4 (Supplementary Fig. S1A and S1B). Oncology drugs such as dabrafenib and trametinib fell into group 1, showing minimal dependence on glucose concentration (Supplementary Fig. S1C). In contrast, fenbendazole and phenformin induced marked, dose-dependent cancer cell death under high or low glucose, respectively, outperforming MAPK inhibitors under equivalent conditions (Supplementary Fig. S1D). We also validated glutamine sensitivity for CM-SLP^{gln} group 4 drugs, niflumic acid and tolfenamic acid, demonstrating their potential as glutamine-dependent repositioned therapies (Supplementary Fig. S2A–S2C). These results suggest that metabolite availability is a crucial determinant of cytotoxicity and drug efficacy of nononcology drugs by dysregulating cancer-related signaling pathways.

Propafenone/low-glucose treatment promotes cancer cell death via the AMPK–mTOR–S6K axis

Cardiovascular disease (CVD) remains a leading global cause of mortality. The overlap between CVD and cancer therapies is increasingly recognized as many anticancer drugs can cause cardiovascular side effects, including arrhythmia (34–36). Additionally, patients with CVD may have an elevated risk of cancer, highlighting the importance of an integrated treatment approach (37). Given that both diseases involve substantial metabolic alterations (38), we aimed to investigate the metabolic association between cancer and

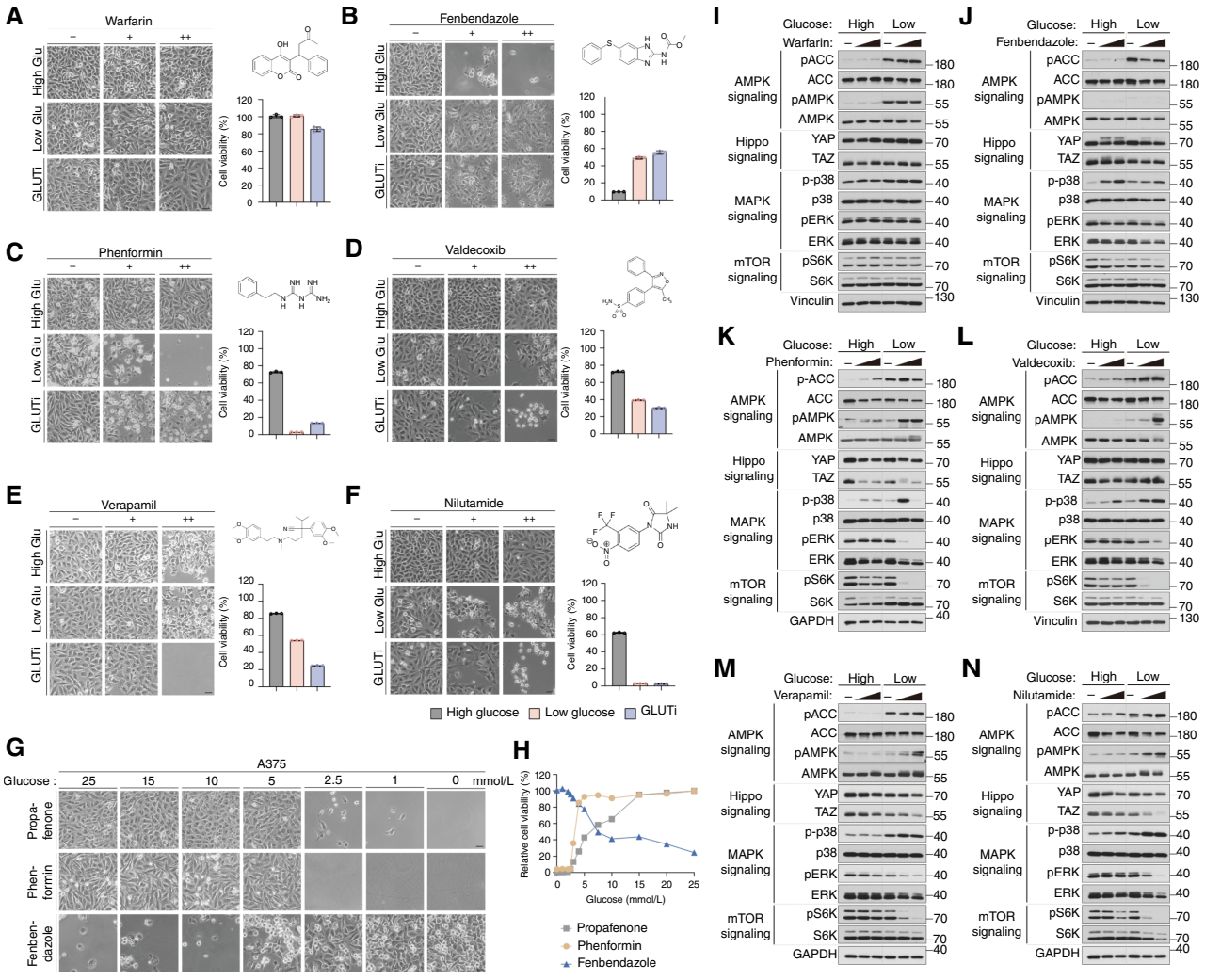

Figure 3.

CM-SLP candidates induce glucose concentration–dependent cytotoxicity and signaling perturbations. **A–F,** Viability of A375 cells subjected to warfarin (group 1; 0, 50, and 100 μmol/L, 8 hours), fenbendazole (group 2; 0, 50, and 100 μmol/L, 8 hours), and group 4 drug (0, 50, and 100 μmol/L, 8 hours) treatment in the presence of high glucose (25 mmol/L), low glucose (1 mmol/L, 11 hours), or the GLUT inhibitor BAY-876 (10 μmol/L), $n = 3$. Scale bars, 30 μm. **G** and **H,** Viability of A375 cells treated with various glucose concentrations (0, 1, 2.5, 5, 10, 15, and 25 mmol/L, 11 hours) combined with either propafenone (30 μmol/L, 24 hours), phenformin (100 μmol/L, 8 hours), or fenbendazole (12.5 μmol/L, 8 hours). Anticancer efficacy of propafenone and phenformin was apparent in <5 mmol/L glucose, whereas it appeared for fenbendazole in >5 mmol/L glucose. **I–N,** Immunoblotting analysis of cancer-related signaling pathways in A375 cells treated with warfarin (**I**), fenbendazole (**J**), phenformin (**K**), valdecoxib (**L**), verapamil (**M**), and nilutamide (**N**) combined with either high (25 mmol/L) or low (1 mmol/L, 11 hours) glucose. –, negative control; low dose, 50 μmol/L; high dose, 100 μmol/L. All drug treatments lasted 8 hours. **I–N,** Lane 1, the control condition; lane 3, drug treatment alone; lane 4, low glucose treatment alone; lane 6, the combination treatment.

CVD. Here, we focused on propafenone, an antiarrhythmic agent identified in CM-SLP^{glu} group 4, as a representative nononcology drug showing markedly increased cytotoxicity under hypoglycemic conditions.

To explore the anticancer efficacy of propafenone under glucose-restricted conditions, we tested the cytotoxic effect of propafenone/hypoglycemia treatment in a wide range of cancer types. In addition to A375 melanoma cells, we tested 786-O renal cancer cells, H358 lung cancer cells, and BT549 breast cancer cells, along with their normal counterparts, HEMn primary epidermal melanocytes, HREC primary renal epithelial cells, BEAS-2B lung epithelial cells, and MCF10A breast epithelial cells. Under glucose-restricted conditions, propafenone exerted dramatic cytotoxicity in all cancer cell lines (**Fig. 4A–D**) but not in their corresponding noncancerous counterparts (**Fig. 4E–H**). This validates the anticancer effect of combined propafenone/hypoglycemia treatment.

To understand the mechanism of this differential cytotoxicity, we analyzed key cancer-related pathways. In cancer cells, the combination of propafenone and low glucose led to marked S6K dephosphorylation, indicative of mTORC1 inhibition, whereas mTORC2-dependent AKT phosphorylation remained unaffected (**Fig. 4I–L**; refs. 39, 40). Additionally, AMPK phosphorylation increased, suggesting pronounced energy stress (41). In contrast,

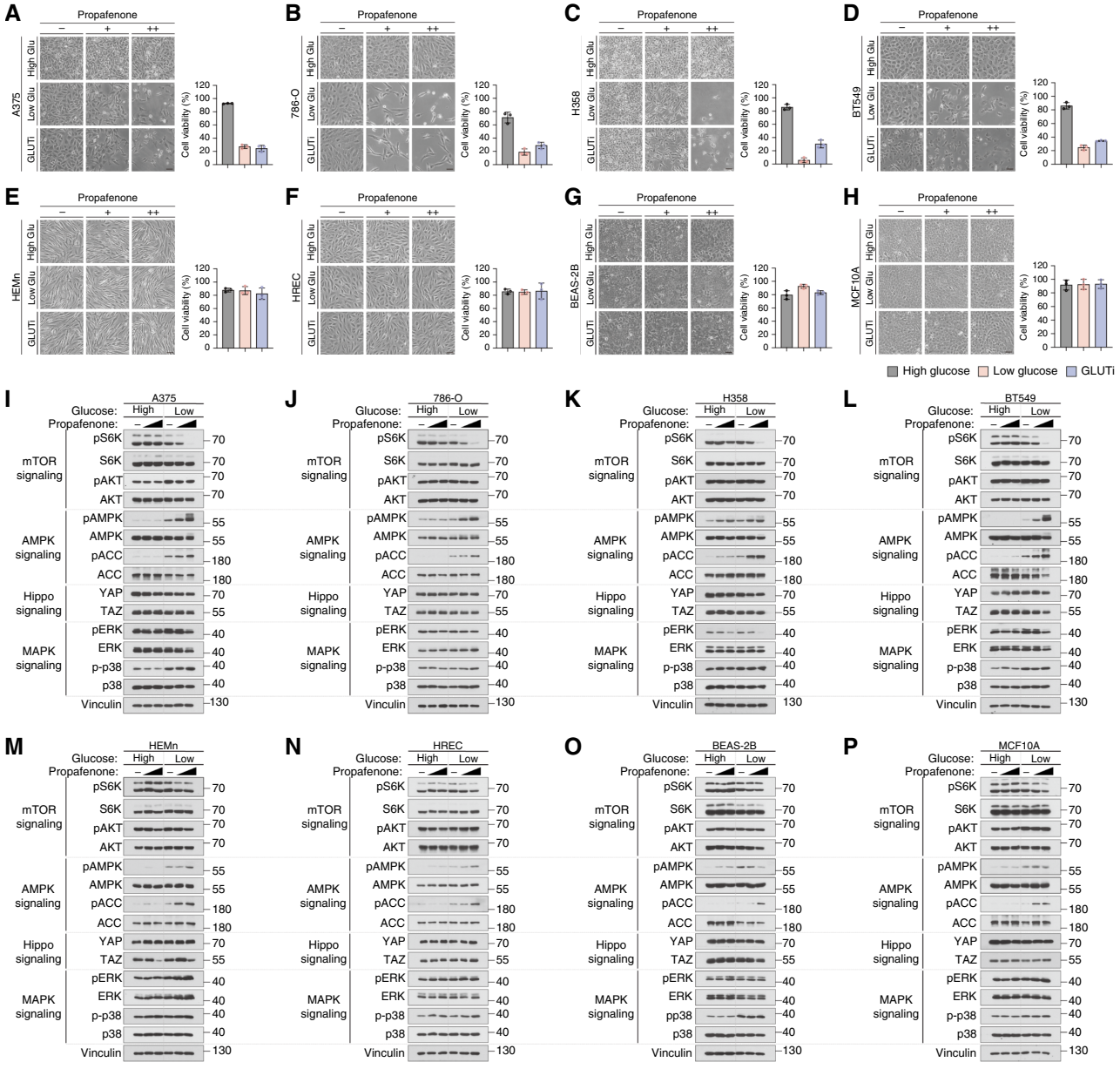

Figure 4.

Propafenone/low-glucose treatment alters oncogenic signaling pathways in cancer cells. **A–D,** Viability of cancer cells subjected to propafenone (0, 10, and 30 μmol/L, 24 hours; 786-O, 48 hours) treatment in the presence of high glucose (25 mmol/L), low glucose (1 mmol/L), or the GLUT inhibitor BAY-876 (10 μmol/L; BT549, 7 μmol/L), $n = 3$. Bottom right, relative viability for each cell type under high/low-glucose concentrations. Scale bars, 30 μm. **E–H,** Viability of normal counterpart cells subjected to propafenone (0, 10, and 30 μmol/L, 24 hours; HREC, 48 hours) treatment in the presence of high glucose (25 mmol/L), low glucose (1 mmol/L), or the GLUT inhibitor BAY-876 (10 μmol/L; MCF10A, 7 μmol/L). Bottom right, relative viability for each cell type under high-/low-glucose concentrations, $n = 3$. **I–P,** Immunoblotting analysis of cancer-related signaling pathways in cells treated with propafenone combined with either high (25 mmol/L) or low (1 mmol/L) glucose. −, negative control; low dose, 10 μmol/L; high dose, 30 μmol/L. A375, HEMn, H358, BES-2B, BT549, and MCF10A were treated for 16 hours. 786-O and HREC cells were treated for 8 hours.

minimal changes were observed in noncancerous cells (**Fig. 4M–P**; Supplementary Fig. S3A), indicating that the energy stress response was largely limited to cancer cells. These findings underscore the AMPK–mTORC1 axis as a key driver of the selective cytotoxicity and highlight its therapeutic potential to target metabolic vulnerabilities in tumors.

Redirecting metabolic interventions toward mTOR-targeted therapies improves the clinical applicability of CM-SLP

Given that TSC2 inhibits mTORC1 upon AMPK activation (42), we investigated its role in the cytotoxic effects of propafenone and low glucose. Using p53-KO MEF cells, p53/TSC2 double-KO MEFs, and TSC2-deficient hepatocellular carcinoma lines, we found that

TSC2 status critically determines treatment response. TSC2 wild-type (WT) MEFs showed strong cytotoxicity with marked AMPK phosphorylation and S6K dephosphorylation under treatment (**Fig. 5A** and **B**). In contrast, TSC2-KO MEFs and TSC2-deficient cells were resistant (**Fig. 5C–E**), showing AMPK activation but no S6K dephosphorylation (**Fig. 5F–H**), indicating that the TSC2–mTORC1 axis is for mediating the cytotoxic effects of propafenone/hypoglycemia treatment. To further dissect the upstream signals, we examined LKB1, a master regulator of AMPK (43). WT HEK293A cells treated with propafenone/low glucose showed robust cell death with AMPK activation and S6K inhibition (**Fig. 5I** and **J**). However, LKB1-KO, A549 (LKB1-deficient), and AMPK-KO cells exhibited diminished responses, with reduced AMPK phosphorylation and minimal S6K dephosphorylation (**Fig. 5K–P**), confirming the critical role of the LKB1–AMPK axis in mediating mTORC1 suppression and cytotoxicity.

Recognizing the clinical limitations of dietary hypoglycemia, we tested mTOR inhibitors as alternative strategies. Both temsirolimus (FDA approved) and Rapalink-1 (third generation; refs. 44, 45) synergized strongly with propafenone, enhancing its anticancer efficacy without glucose restriction (**Fig. 5Q** and **R**). These findings suggest that integrating mTOR inhibitors into treatment regimens could overcome the challenges associated with dietary interventions, making the therapies more clinically applicable. As temsirolimus and everolimus are approved for patients with renal cell carcinoma (46, 47), we validated our approach *in vivo* using NOD/SCID gamma mice bearing 786-O tumors. Mice received propafenone (30 mg/kg), temsirolimus (0.3 mg/kg), or glucose uptake inhibitor BAY-876 (2 mg/kg; ref. 48), either alone or in combination, every other day for 30 days. Remarkably, combinations of propafenone/BAY-876 and propafenone/temsirolimus significantly reduced tumor size and weight with no adverse effects on body weight (**Fig. 5S** and **T**).

Collectively, these findings demonstrate that the anticancer effect of propafenone/low-glucose treatment is mediated by the LKB1–AMPK–TSC2–mTORC1 axis. Moreover, combining propafenone with mTOR inhibitors offers a feasible alternative for patients unable to undergo dietary interventions. These findings, guided by CM-SLP, support personalized oncometabolic therapy targeting cancer-specific vulnerabilities.

Propafenone targets the K_{Ca} channel to inhibit AMPK–mTOR axis and promote cancer cell death

To identify the molecular targets responsible for the propafenone/low-glucose efficacy, we first examined voltage-gated sodium (Na_v) channel, the known target of propafenone in cardiac cells. However, 786-O cells lacked Na_v expression (Supplementary Fig. S3B). We then evaluated other potential antiarrhythmic drug targets and found no detectable voltage-gated calcium (Ca_v) or potassium channels (Supplementary Fig. S3C; **Fig. 6A**). Interestingly, we observed high expression and functional activity of large-conductance calcium-activated potassium channels (BK channels), a subtype of K_{Ca} channels, in 786-O cells (**Fig. 6B** and **C**). Cancer Cell Line Encyclopedia (CCLE) database analysis further confirmed K_{Ca} channel expression in other cancer lines used in our study (Supplementary Fig. S3D–S3G; ref. 49).

Next, patch-clamp assays revealed significant inhibition of K_{Ca} channel activity not only with propafenone but also with other antiarrhythmic drugs like verapamil (**Fig. 6D–F**), suggesting broader utility for antiarrhythmic drugs in CM-SLP^{glu} group 4. Similarly, BK-specific inhibitors (paxilline), as well as pan-K_{Ca} inhibitors (TEA and Tram-34), effectively suppressed K_{Ca} activity (**Fig. 6D–F**) and induced strong cytotoxicity under glucose restriction, mimicking propafenone (**Fig. 6G–J**). All agents inhibited mTORC1 and increased AMPK phosphorylation (**Fig. 6K–N**), supporting a shared mechanism of energy stress–induced mTOR inhibition to promote cancer cell death. Following these results, we tested other CM-SLP group antiarrhythmics (Supplementary Fig. S4A and S4B). Amiodarone (group 3) strongly inhibited K_{Ca} channel (Supplementary Fig. S4C and S4D), induced cytotoxicity, and suppressed mTOR signaling even without glucose restriction (Supplementary Fig. S5A and S5B). In contrast, group 1 drugs, as well as procainamide, did not induce sufficient K_{Ca} channel inhibition (Supplementary Fig. S4C and S4D). Neither did these drugs induce significant cell death (Supplementary Fig. S5C–S5K) nor inhibit mTOR signaling (Supplementary Fig. S5L–S5T). These findings highlight K_{Ca} channel inhibition as a specific and actionable target. Next, to confirm specificity, we tested PAP-1 (voltage-gated K^+ channel inhibitor), which did not affect cell viability, AMPK–mTOR signaling, or K_{Ca} activity (Supplementary Fig. S6A–S6D; ref. 50), validating the role of K_{Ca} channels.

Given that AMPK is a well-established energy stress sensor, we hypothesized that K_{Ca} inhibition under glucose restriction would augment energy stress. To test this, we measured ATP production rates under various treatment conditions (51). Our results showed synergistic ATP depletion with propafenone and paxilline under the low-glucose level (**Fig. 6O** and **P**). These findings align with previous reports that K_{Ca} channel inhibition reduces calcium flux into mitochondria, impairing ATP synthesis (52).

Together, our results demonstrate that K_{Ca} channel inhibition combined with glucose restriction intensifies energy stress and promotes cell death via the LKB1–AMPK–TSC2–mTORC1–S6K signaling axis (**Fig. 6Q**). Because the K_{Ca} channel *KCNMA1* gene is frequently amplified in cancer (53, 54), these findings suggest a therapeutic niche for K_{Ca} inhibitors in metabolically vulnerable cancers. Although we demonstrated anticancer efficacy of propafenone/hypoglycemia, its effect in CVD models remains unexplored, warranting future investigation into its dual anticancer and cardioprotective potential.

Biguanide/low glucose impairs metabolic plasticity and Hippo–YAP signaling in cancer cells

Next, we investigated the molecular mechanism of phenformin, a top-scoring CM-SLP^{glu} group 4 biguanide, to validate its anticancer efficacy under glucose-restricted conditions and identify alternative targets that could serve as substitutes for hypoglycemia. We first confirmed cancer-selective cytotoxicity of biguanide/low glucose across cancer and normal counterparts to daily cycles of combined treatment. Despite varied sensitivity, metformin consistently caused cell death in cancer cells, but not in normal counterparts, under glucose restriction (**Fig. 7A**). To understand the combined effect on energy metabolism, we analyzed the ATP production rate from glycolysis and OXPHOS (**Fig. 7B**). Importantly, neither treatment alone impaired ATP levels. Metformin treatment shifted ATP production toward glycolysis, whereas glucose restriction favored OXPHOS, demonstrating the metabolic plasticity of cancer cells. These results indicate that a significant reduction in ATP levels could be achieved by biguanide/low glucose (**Fig. 7C**).

To test whether ATP restoration rescues cell death, we supplemented fructose, which bypasses pentose phosphate pathway and hexosamine pathway and feeds into glycolytic pathway via GLUT2/5 (Supplementary Fig. S7A). This provides cells an alternative way to

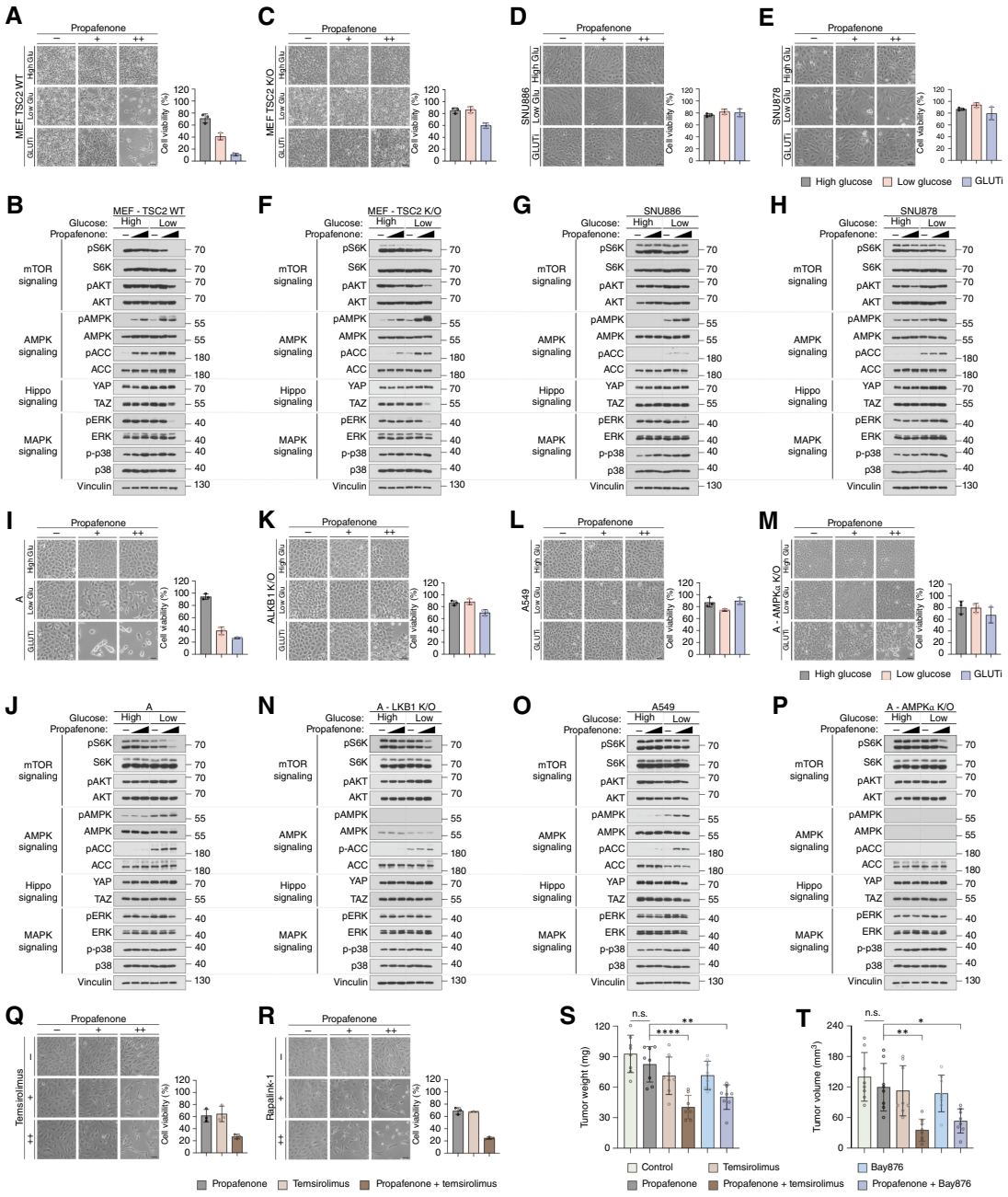

Figure 5.

LKB1–AMPK–TSC2–mTOR pathway mediates propafenone-/low glucose–induced anticancer efficacy. **A,** Viability of TSC2 WT MEF cells treated with propafenone (0, 5, and 15 μmol/L, 24 hours) under high glucose (25 mmol/L), low glucose (1 mmol/L), or GLUT inhibitor BAY-876 (2 μmol/L). **B,** Immunoblotting of cancer signaling pathways in TSC2 WT MEFs treated with propafenone and high or low glucose. −, untreated; low dose, 5 μmol/L; high dose, 15 μmol/L; 4-hour treatment. **C–E,** Viability of indicated cells after propafenone treatment (0, 5, 15 μmol/L, 24 hours) under high/low glucose or BAY-876 (2 μmol/L). **F–H,** Immunoblotting of cells in **C–E** treated with propafenone ± glucose. −, untreated; low dose, 5 μmol/L; high dose, 15 μmol/L; 4-hour treatment. **I,** Viability of HEK293A cells treated with propafenone (0, 10, and 20 μmol/L, 24 hours) with high/low glucose or BAY-876 (10 μmol/L). **J,** Immunoblotting in HEK293A cells treated as in **I**. −, untreated; low dose, 5 μmol/L; high dose, 15 μmol/L; 4-hour treatment. **K–M,** Viability of LKB1-/AMPK-KO HEK293A and A549 cells treated with propafenone (0, 10, and 20 or 30 μmol/L, 24 hours) under high/low glucose or BAY-876 (10 μmol/L). **N–P,** Immunoblotting of cells in **K–M** treated with propafenone ± glucose. −, untreated; low dose, 10 μmol/L; high dose, 20 μmol/L; HEK293A, 2 hours; A549, 16 hours treatment. **Q** and **R,** Viability of 786-O cells treated with propafenone (10 or 30 μmol/L), temsirolimus (100 or 300 nmol/L), or rapalink-1 (1 or 3 nmol/L), alone or in combination (72 hours, $n = 3$). **S** and **T,** *In vivo* xenograft tumor growth measured by tumor weight (mg) and volume (mm^3) after administration of the combinations of propafenone/temsirolimus or propafenone/BAY-876. All mouse groups had $n = 8$. **A**, **C–E**, **I**, and **K–M,** bottom right, relative viability for each cell type under high-/low-glucose concentrations, $n = 3$. Scale bars, 30 μm. *, $P < 0.05$; **, $P < 0.01$; ****, $P < 0.0001$; n.s., nonsignificant.

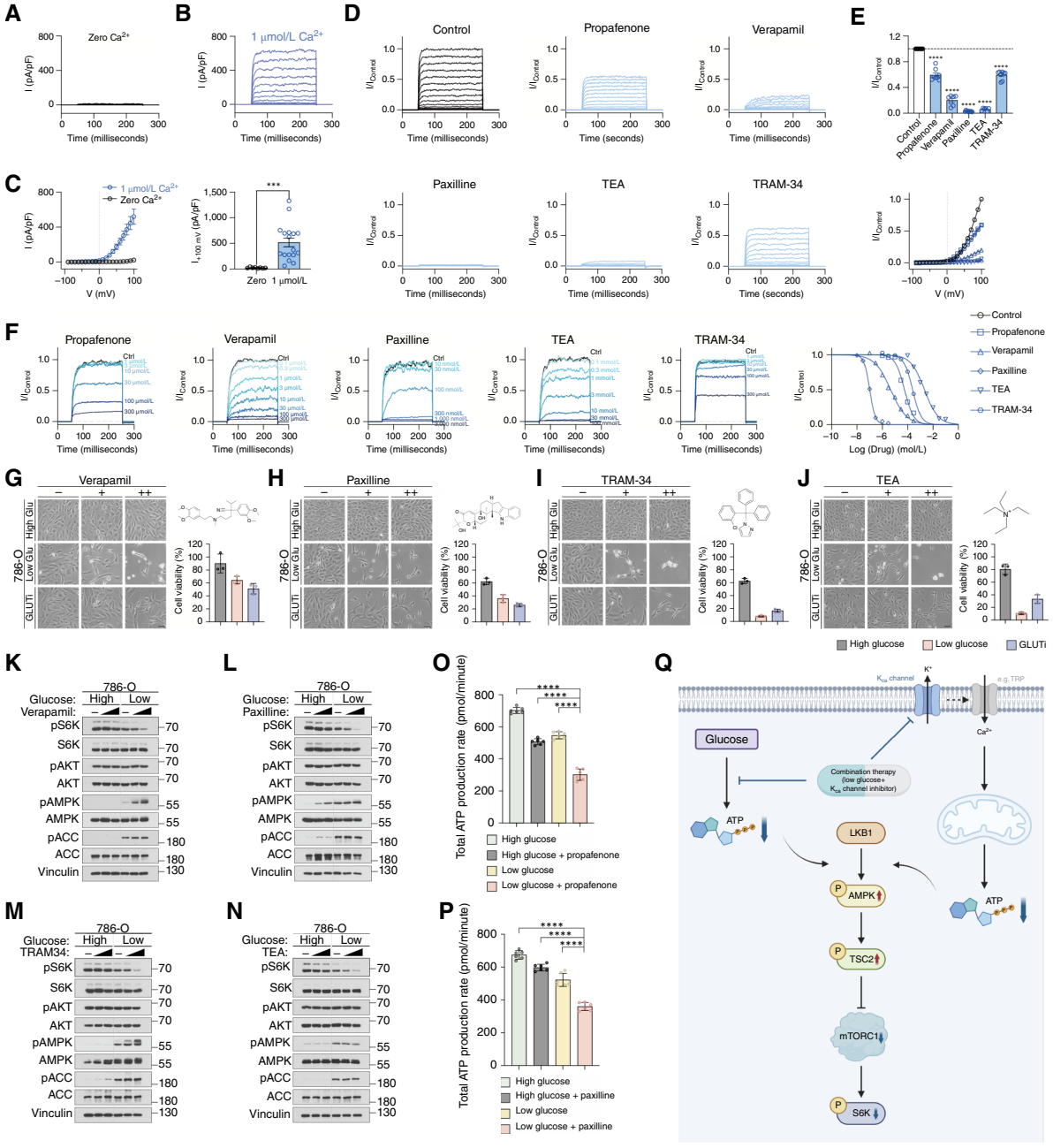

Figure 6.

Propafenone targets the K_{Ca} channel to inhibit the AMPK–mTOR axis and promote cancer cell death. **A** and **B,** Representative whole-cell K^+ currents in 786-O cells with intracellular Ca^{2+} fixed at 0 μmol/L (**A**) or 1 μmol/L (**B**). **C,** Voltage–current relationship and current density at 100 mV in 0 μmol/L (24.33 ± 3.73 pA/pF, $n = 8$) or 1 μmol/L Ca^{2+} (519.91 ± 87.22 pA/pF, $n = 17$). **D,** Normalized K^+ currents with extracellular addition of propafenone (20 μmol/L), verapamil (20 μmol/L), paxilline (20 μmol/L), TEA (20 mmol/L), or TRAM-34 (60 μmol/L), with intracellular Ca^{2+} fixed at 1 μmol/L. **E,** Peak current densities at 100 mV: propafenone, 0.594 ± 0.090 ($n = 8$); verapamil, 0.201 ± 0.029 ($n = 7$); paxilline, 0.029 ± 0.003 ($n = 9$); TEA, 0.060 ± 0.009 ($n = 6$); and TRAM-34, 0.592 ± 0.024 ($n = 8$). **F,** Dose–response curves with IC_{50} values: propafenone, 56.94 ± 1.04 μmol/L ($n = 9$); verapamil, 4.60 ± 0.10 μmol/L ($n = 8$); paxilline, 102.0 ± 1.0 nmol/L ($n = 9$); TEA, 2.14 ± 0.01 mmol/L ($n = 9$); and TRAM-34, 247.6 ± 5.6 μmol/L ($n = 9$), with intracellular Ca^{2+} fixed at 1 μmol/L. **G–J,** Viability of 786-O cells treated with verapamil (0, 10, and 30 μmol/L), paxilline (0, 10, and 20 μmol/L), TRAM-34 (0, 10, and 30 μmol/L), or TEA (0, 10, and 30 mmol/L) for 48 hours under high (25 mmol/L) or low (1 mmol/L) glucose or BAY-876 (3 μmol/L). Top right, structures; bottom right, viability summarized ($n = 3$). **K–N,** Immunoblotting of signaling pathways in 786-O cells treated as in **G–J** for 8 hours under high or low glucose. **O** and **P,** Total ATP production in 786-O cells after 24 hours treatment with propafenone (40 μmol/L) or paxilline (20 μmol/L) in high or low glucose ($n = 6$). **Q,** Schematic of the LKB1–AMPK–TSC2–mTORC1–S6K axis mediating selective cytotoxicity of propafenone under glucose-limited conditions. ***, $P < 0.001$; ****, $P < 0.0001$.

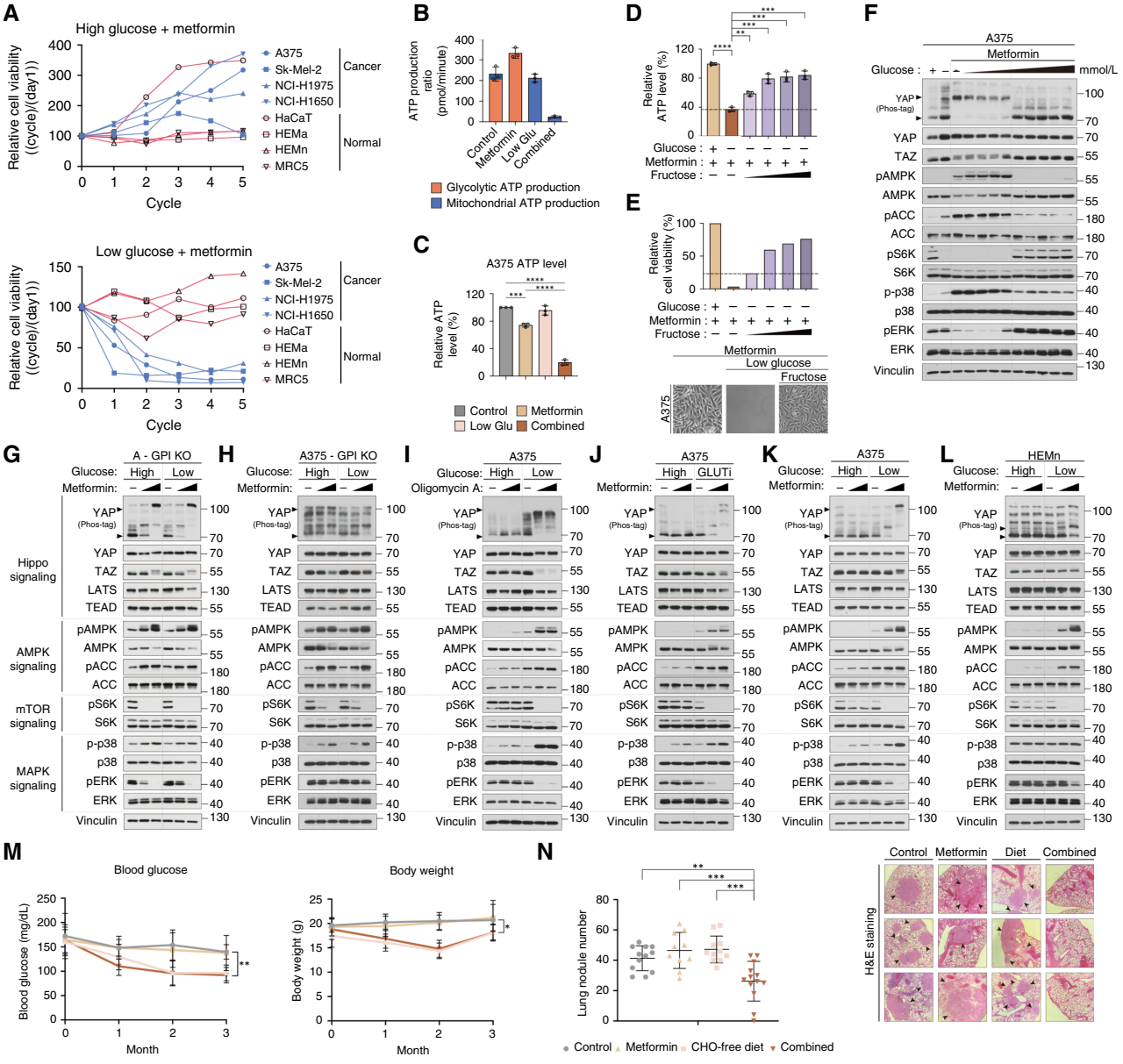

Figure 7.

Biguanide/low glucose impairs metabolic plasticity and Hippo–YAP signaling in cancer cells. **A,** Relative viability of cancer and normal cells after daily 24-hour cycles of metformin (10 mmol/L) in either high (25 mmol/L) or low (1 mmol/L) glucose. Viability was normalized first to glucose-only control at each time point and then to the baseline (cycle 0). **B,** Measurements of real-time ATP production (pmol/minute) in A375 cells subjected to either metformin alone, low glucose alone, or in the two in combination. **C,** Measurements of relative intracellular ATP levels in A375 cells treated as in **B**. **D** and **E,** Viability and ATP levels in A375 cells after fructose supplementation (25–200 mmol/L). Scale bars, 30 μm. **F,** Immunoblotting analysis of A375 cells treated with various glucose concentrations (0.5, 1, 2, 2.5, 5, 10, 15, 20, and 25 mmol/L, 11 hours) combined with metformin (10 mmol/L, 8 hours). Glucose concentrations are lower than 2.5 mmol/L and synergized with metformin to disrupt cell signaling. Arrowheads, YAP phosphorylation status. **G** and **H,** Immunoblotting of GPI-KO HEK293A cells (**G**) and A375 cells (**H**) treated with metformin (0, 3, and 10 mmol/L, 8 hours) under high (25 mmol/L) or low (1 mmol/L, 11 hours) glucose. **I,** Immunoblotting analysis of signal pathway perturbations in A375 cells treated with oligomycin A (0, 1, and 5 μmol/L, 8 hours) combined with high (25 mmol/L) or low glucose (1 mmol/L, 11 hours). **J,** Immunoblotting analysis of A375 cells treated with metformin (0, 3, and 10 mmol/L, 8 hours) combined with high glucose (25 mmol/L) or the GLUT inhibitor BAY-876 (10 μmol/L, 11 hours). **K** and **L,** Immunoblotting analysis of A375 cells and HEMn cells treated with metformin (0, 3, and 10 mmol/L, 8 hours) in high (25 mmol/L) or low glucose (1 mmol/L, 11 hours). **M,** Measurements of blood glucose levels (mg/dL) and body weights (g) from each group for 3 months. **N,** Number of lung tumor nodules counted from each experimental group. Lung nodules were counted using microscopy in representative images of hematoxylin and eosin (H&E)–stained lungs from each mouse group. Black arrows, tumor nodules. **C–E,** Statistical analysis was performed using one-way ANOVA with Bonferroni correction. *, $P < 0.05$; **, $P < 0.01$; ***, $P < 0.001$; ****, $P < 0.0001$.

produce ATP even under conditions that impair both glucose uptake and OXPHOS (**Fig. 7D**). Fructose restored ATP and viability dose-dependently, indicating that biguanide/low glucose causes cell death via energy crisis (**Fig. 7E**). Importantly, glucose below 5 mmol/L was sufficient to disrupt key signaling pathways to induce cancer death, suggesting that biguanide synergize with physiologically relevant hypoglycemic conditions (**Fig. 7F**). Mechanistically, depletion of GPI, OXPHOS inhibition, or GLUT blockade, which impairs glycolytic ATP production, elicited biguanide-induced signaling perturbations even in high glucose (**Fig. 7G–J**), confirming that biguanides/low glucose impairs metabolic plasticity between glycolysis and OXPHOS.

Next, we explored how biguanide/hypoglycemia differentially affects signaling pathways in cancer versus normal cells. Metformin alone had minimal effects, but under low glucose, it disrupted multiple cancer signaling pathways, indicating energy depletion, cellular stress, and growth suppression (**Fig. 7K**; Supplementary Fig. S7B–S7H). Surprisingly, in normal cells, metformin/low glucose recapitulated similar pathway perturbations, except for Hippo pathway–induced YAP/TAZ inhibition (**Fig. 7L**; Supplementary Fig. S7I). As YAP and TAZ are oncogenic transcriptional coactivators of the Hippo pathway (55, 56), their cancer cell–selective destabilization explains the differential cytotoxicity of biguanide/low glucose (57, 58).

To validate *in vivo* efficacy, we treated the K-Ras^{LA2} lung cancer model with metformin and either a normal or carbohydrate-free diet. The carbohydrate-free diet alone reduced blood glucose and body weight, whereas metformin alone or in combination did not further affect these parameters (**Fig. 7M**), consistent with prior reports (59). Importantly, the antitumor effect of metformin was highly dependent on blood glucose level. It showed little benefit alone or with a normal diet but synergized with carbohydrate-free diet under hypoglycemia to dramatically suppress tumor growth (**Fig. 7N**). Furthermore, our results not only resolve the controversial anticancer effect of the biguanides (60) but also strengthen previous reports by demonstrating that biguanides are one of the most prominent drugs that synergize with the hypoglycemic condition (61, 62).

Biguanide/low glucose targets YAP-driven cancer cells via the ATP–FAK–RhoA–LATS axis

We next investigated how biguanide/glucose restriction links ATP depletion to YAP inhibition. Morphologically, cancer cells showed shrinkage and disrupted focal adhesions, implicating impaired integrin–FAK signaling and F-actin remodeling as part of energy stress–induced cytotoxicity (**Fig. 8A** and **B**). Fructose supplementation restored ATP levels, rescuing FAK activation, LATS inhibition, and YAP/TAZ activation via dephosphorylation (**Fig. 8C**). To assess the role of the RhoA–Hippo axis, we expressed constitutively active RhoA and depleted LATS1/2, both of which blocked YAP/TAZ phosphorylation induced by biguanide/low glucose (**Fig. 8D** and **E**). Interestingly, AMPK depletion failed to reverse YAP/TAZ inhibition, indicating that the effect is independent of AMPK (**Fig. 8F**). Hippo pathway–induced YAP phosphorylation subsequently led to its cytoplasmic translocation (**Fig. 8G**), disrupted YAP–TEAD interaction, and reduced TEAD target gene expression critical for tumor progression (**Fig. 8H–J**). These findings suggest that impaired metabolic plasticity by biguanide/low glucose triggers cell death via the FAK–RhoA–LATS–YAP/TAZ–TEAD axis (**Fig. 8K**).

Because YAP and TAZ mediate biguanide-/low glucose–induced cancer cell death, it is conceivable that the combined treatment induces minimal cytotoxicity in YAP-/TAZ-deficient (YAP^{low}) cancer cells. Although the protumorigenic role of YAP/TAZ is well established in various solid tumors, hematologic malignancies and small cell lung cancer (SCLC) cells hardly express YAP/TAZ (63, 64). Notably, SCLC and hematologic cancers with minimal YAP/TAZ expression showed resistance to biguanide/low glucose, unlike YAP^{high} cells, indicating that YAP/TAZ expression is an indicator of cell vulnerability to the biguanide/low-glucose combination therapy (**Fig. 8L**). We also tested Hippo-inactive (Hippo^{OFF}/YAP^{ON}) cancers such as 92.1 uveal melanoma and y-MESO-26B mesothelioma. These cells, which express constitutively active YAP, were resistant to treatment compared with Hippo WT cells (**Fig. 8M**). Thus, cancers with disrupted Hippo signaling are less responsive to therapy. To address this limitation, we propose targeting TEAD directly using YAP–TEAD inhibitors to bypass the need for Hippo kinase activity.

Redirecting metabolic intervention toward YAP–TEAD–targeted therapies improves the clinical applicability of CM-SLP

Because it remains challenging to apply hypo-nutrient interventions in patients, we explored alternative means to exploit targeted therapies suggested by CM-SLP^{glu} that would improve their clinical applicability. As Hippo and YAP status determines sensitivity to biguanide/hypoglycemia, we developed a small-molecule inhibitor targeting the YAP–TEAD complex to bypass dietary restrictions and further target Hippo^{OFF}/YAP^{ON} cancers. A computer-based screen identified BMY-123, which binds TEAD interface 3, disrupting YAP/TAZ–TEAD interactions (Supplementary Fig. S8A and S8B; ref. 65). Using FMO analysis, we found key TEAD1 residues (E368, E393, and D249) mediating this interaction (Supplementary Fig. S8C), with electrostatic and hydrophobic interactions critical for its binding (Supplementary Fig. S8D). BMY-123 bound TEAD1 directly with a KD of 24.1 μmol/L (Supplementary Fig. S8E).

We then tested whether BMY-123 could substitute for hypoglycemia to synergize with biguanides. The combination of biguanide/BMY-123 treatment potently dissociated YAP/TAZ from TEAD (Supplementary Fig. S8F) and significantly inhibited TEAD reporter activity and target gene expression (Supplementary Fig. S8G). Consistent with these results, phenformin/BMY-123 cotreatment enhanced cytotoxicity beyond BMY-123 alone, mimicking biguanide/hypoglycemia effects (Supplementary Fig. S8H). Importantly, this combination induced cytotoxicity in previously resistant Hippo^{OFF}/YAP^{ON} cells, including 92.1 uveal melanoma cells that were insensitive to biguanide/low-glucose treatment (**Fig. 8M**; Supplementary Fig. S8H). Notably, Hippo^{OFF}/YAP^{ON} cells showed an even lower IC_{50}, possibly because of their YAP-dependency. In addition, the treatment markedly improved selectivity for cancer cells compared with their normal counterparts (Supplementary Fig. S8H).

To verify the *in vivo* efficacy of biguanide/BMY-123 treatment, we treated K-Ras^{LA2} mice with metformin and BMY-123, both alone and in combination. The combination significantly enhanced anticancer effects, replicating the metformin/hypoglycemia efficacy even in the absence of dietary intervention (Supplementary Fig. S8I). Furthermore, phenformin synergized effectively not only with BMY-123 but also flufenamic acid and VT107, which are well-established YAP–TEAD inhibitors currently in clinical trials (Supplementary Fig. S8J–S8L; refs. 66, 67). These results underscore the importance of Hippo pathway status in biguanide/hypoglycemia response and demonstrate that TEAD inhibitors

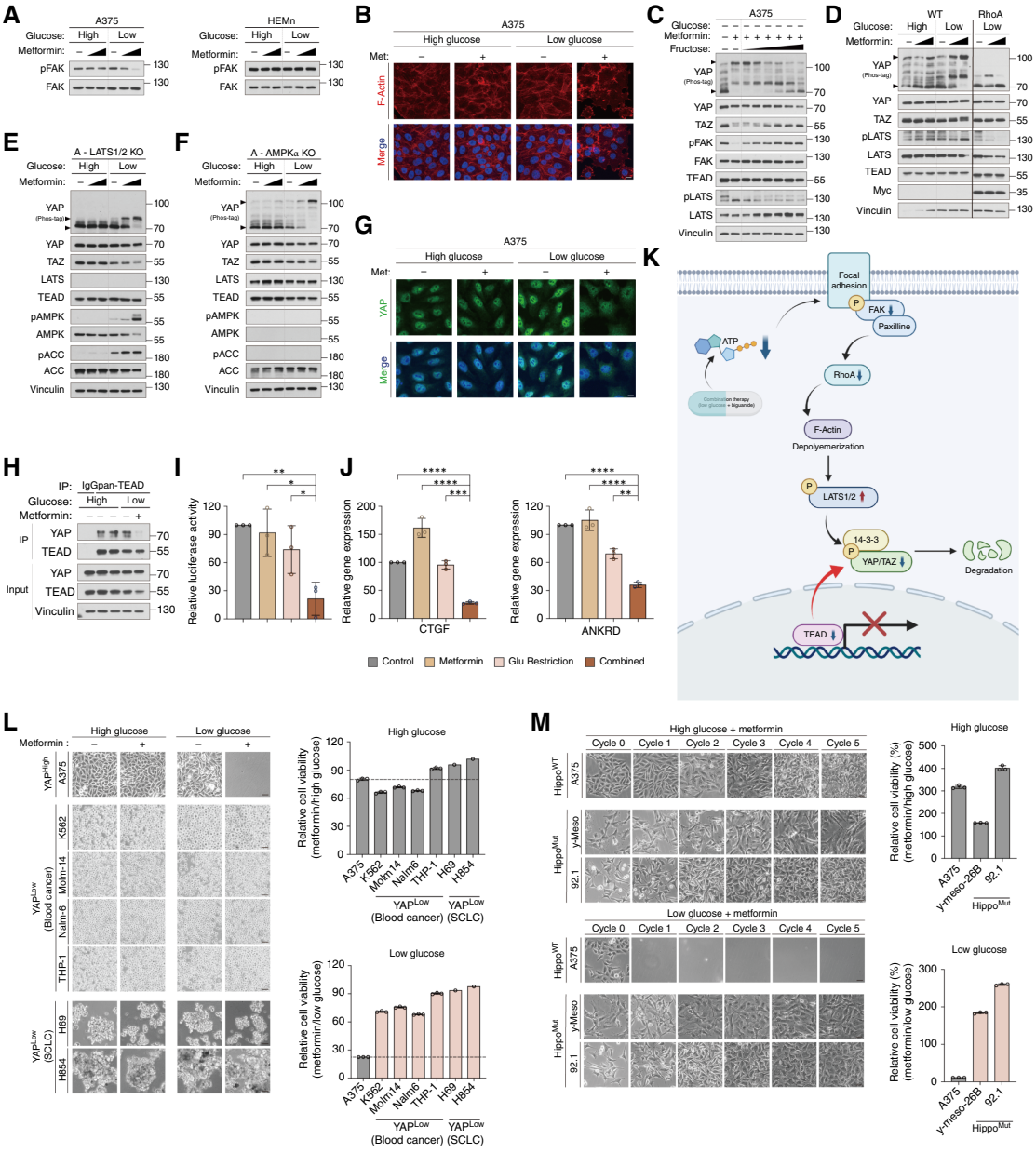

Figure 8.

Biguanide/low glucose targets YAP-driven cancer cells via the ATP–FAK–RhoA–LATS axis. **A,** Immunoblotting of FAK phosphorylation in A375 and HEMn cells treated with metformin (0, 3, and 10 mmol/L, 8 hours) under high (25 mmol/L) or low (1 mmol/L) glucose (11 hours). **B,** Immunofluorescence of F-actin in A375 cells under same conditions. Red, phalloidin; blue, DAPI. Scale bars, 15 μm. **C,** Immunoblotting analysis of lysates derived from A375 cells treated with metformin (0, 3, and 10 mmol/L, 8 hours) in low glucose (1 mmol/L, 11 hours) supplemented with fructose (10, 25, 50, 100, 150, and 200 mmol/L). **D,** Immunoblotting analysis of YAP and LATS dephosphorylation induced via ectopic RhoA expression in HEK293A cells treated with metformin (0, 3, and 10 mmol/L, 8 hours) in high (25 mmol/L) or low glucose (1 mmol/L, 11 hours). **E** and **F,** Immunoblotting analysis of YAP phosphorylation status in LATS1/2- or AMPKα-KO HEK293A cells treated as above. **G,** Immunofluorescence analysis of YAP cytoplasmic translocation in A375 cells treated as above. Green, YAP; blue, DAPI. **H,** Immunoprecipitation analysis of the interaction between YAP and TEAD in the cell lysates used in **G**. **I,** TEAD luciferase reporter activity (8x GTIIC) in HEK293A cells subjected to metformin/low-glucose treatment. *Y*-axis, relative luciferase units (RLU), $n = 3$. **J,** qRT-PCR analysis of the TEAD target genes CTGF and ANKRD1 in HEK293A cells subjected to metformin/low-glucose treatment, $n = 3$. **K,** Illustration of the ATP–FAK–RhoA–LATS–YAP/TAZ–TEAD pathway underlying cancer cell–specific cytotoxicity of biguanide/low glucose. **L,** Viability of YAP^{high} and YAP^{low} cancer cells treated with metformin in high (25 mmol/L) or low glucose (1 mmol/L). YAP^{high} cell line, A375; YAP^{low} cell lines, the K562, Molm-14, Nalm-6, and THP-1 blood cancer cell lines, as well as the NCI-H69 and NCI-H854 SCLC cell lines. Scale bars, 30 μm. **M,** Viability of $Hippo^{OFF}/YAP^{ON}$ cancer cells treated with metformin in high (25 mmol/L)- or low (1 mmol/L)-glucose media. $Hippo^{OFF}/YAP^{ON}$ cancer cell lines, y-meso-26B mesothelioma and 92.1 uveal melanoma cell lines. **I,** Statistical analysis was performed using a *t* test; **J,** statistical analysis was performed using one-way ANOVA with Bonferroni corrections for multiple comparisons. *, $P < 0.05$; **, $P < 0.01$; ***, $P < 0.001$; ****, $P < 0.0001$.

can broaden clinical applicability of CM-SLP–based strategies by identifying targetable metabolic vulnerabilities and combinatorial therapies.

Discussion

In this study, we introduced CM-SLP, a metabolite-dependent high-throughput screening platform designed to repurpose FDA-approved drugs based on unexpected cytotoxicity and metabolic vulnerabilities under altered nutrient availability. Our results expand the current concept of precision medicine toward individualized medication guidelines that depend on each cancer patient's metabolic state. Emerging evidence shows that cancer metabolism significantly influences drug response, with systemic and tumor-specific metabolic changes shaping treatment efficacy (4, 6, 68). Although metabolic syndromes (hyper-nutrient states) increase cancer risk, dietary interventions (hypo-nutrient states) such as IF enhance anticancer drug efficacy (24, 69, 70). Hence, CM-SLP provides a comprehensive resource for the analysis and prediction of an individual cancer patient's drug response according to their metabolic status. CM-SLP offers a resource to predict individual drug responses according to metabolic status, identifying non-oncology and oncology drugs with unrecognized efficacy or toxicity under specific nutrient conditions. In addition to repositioning nononcology drugs for patients with cancer, CM-SLP also suggested the possibility that metabolic status may explain unwanted cytotoxicity from nononcology drugs in patients without cancer.

Previous research has shown that nutrient levels in the blood plasma and microenvironmental tumor interstitial fluid (TIF) dictate nutrient availability in cancer cells (71–73). Factors such as tumor type, epigenetic state, anatomic location, tumor microenvironment, and other cellular components can affect cancer cell metabolism. Importantly, as systemic metabolism alters TIF composition, metabolic syndromes and dietary interventions likely modulate tumor nutrient levels, explaining the synergy with group 2 and 4 CM-SLP candidates. Future studies should clarify how cancer cells respond to CM-SLP drugs under diverse systemic and local metabolic conditions. Additionally, developing standardized methods to assess individual metabolic profiles could help guide CM-SLP–based therapies.

Among tested metabolites, glucose emerged as the strongest driver of differential drug responses, preferentially sensitizing cancer cells. Although other studies have highlighted glutamine or fatty acids, we observed glucose as the key modulator of drug-induced cytotoxicity in multiple cancer types. It is noteworthy that distinct cancer types may respond with different CM-SLP scores for each condition. Moreover, although most studies have examined how reducing glucose levels potentiates drug responses, we initiated a follow-up study on the group 2 drug fenbendazole, which exhibited unexpected cytotoxicity only under hyperglycemia. It is important to note that glucose concentrations above 10 mmol/L (180 mg/dL) were required for fenbendazole to induce significant cytotoxicity, suggesting its therapeutic potential for hyperglycemic patients with cancer. This is, to our knowledge, the first demonstration of high glucose enhancing nononcology drug efficacy. These results align with findings that hyperglycemia potentiates chemotherapy in pancreatic cancer (bioRxiv 2022.04.29.490090). Similarly, several CM-SLP drugs showed enhanced or suppressed anticancer effects depending on metabolite concentrations, emphasizing the need for further research into nutrient-sensitive drug repurposing.

Although hyper-nutrient conditions are clinically accessible, hypo-nutrient environments that synergize with group 4 drugs are challenging to achieve in patients with cancer (70). Thus, it is critical to identify downstream pathways mediating cancer-selective cytotoxicity in order to substitute dietary interventions with readily applicable targeted therapies. Surprisingly, group 4 CM-SLP^{glu} scores indicate that, among FDA-approved drugs, glucose restriction confers significant cytotoxicity to propafenone and biguanides. We found that dual inhibition of glycolysis and calcium flux, achieved via propafenone/hypoglycemia, induced energy stress in cancer cells. Clarifying the mechanisms, we found that targeted treatment with temsirolimus, an mTOR inhibitor, could partially substitute for hypoglycemia. Similarly, we and others found that dual inhibition of glycolysis and OXPHOS, achieved via biguanides/hypoglycemia, suppressed metabolic plasticity and ATP production. Additionally, consistent with prior findings, CM-SLP independently confirmed metformin as a highly glucose-sensitive drug (61, 62, 74). It is well known that cancer cells, in contrast to normal cells, typically exhibit a much higher proliferation rate and greater dependency on ATP, which may partially explain the cancer-specific effects of these combinations (75, 76). Further clarifying the mechanisms, we found that targeted treatment with BMY-123, which disrupts the YAP–TEAD complex, could partially replace the hypoglycemic requirement. Although Hippo^{OFF}/YAP^{ON} status renders cancer cells insensitive to the biguanide/low-glucose combination, the alternative biguanide/TEAD inhibitor combination allowed us to overcome this limitation. However, as drug–nutrient interactions were studied in simplified metabolite conditions, caution is needed in extrapolating these findings to clinical settings in which metabolic interactions are more complex.

Here, we performed a large-scale screen to identify anticancer uses of nononcology FDA-approved drugs, focusing on those with differential cytotoxicity in hyper- and hypo-metabolite conditions. These drugs, even safe at higher doses, showed minimal toxicity alone but significant cancer-specific efficacy under tailored metabolic conditions. Given the large number of drug repurposing candidates with unexpected metabolite dependencies that emerged in this initial screen, we aim to expand CM-SLP approach toward various cancer types, metabolites, and mouse models. Although CM-SLP presents a promising approach for understanding metabolic context in drug sensitivity, the extension of this platform to personalized medicine would require integration with *in vivo* nutrient profiling, patient-specific metabolic states, and tumor-derived models to fully reflect clinical complexity. In addition to the immediate repurposing of existing drugs for anticancer indications, the CM-SLP database introduces a framework that can guide the way to a treatment modality we refer to as oncometabolic precision medicine. The idea is to provide medication guidelines for individual patents based on metabolite concentrations in their blood or tumor microenvironments. This will help diversify anticancer treatment modalities and maximize the safety and efficacy of such treatments. Our CM-SLP results further suggest that, during preclinical and clinical trials, drug efficacy and cytotoxicity should be examined under key representative metabolic conditions to improve clinical decision-making.

Data Availability

All raw data generated during this study are available from the corresponding author upon reasonable request. Publicly available datasets analyzed in this study were obtained from the CCLE (https://sites.broadinstitute.org/ccle).

Authors' Disclosures

K.-L. Guan reports potential financial interest and/or service on advisory board of the following companies: Vivace Therapeutics, OncoC4, Inc., Innocare Pharma, Shanghai Henlius Biotech, Meton Pharmaceuticals, and Cullgen. T. Hashimoto reports personal fees from Myriad Genetics, Inc., Takata Pharmaceutical, Miyarisan, and CytoGen and other support from Guardant Health outside the submitted work. T. Yoshino reports grants from Amgen K.K., Bristol Myers Squibb K.K., Caris MPI, Inc., Daiichi Sankyo Co., Ltd., Eisai Co., Ltd., Exact Sciences Corporation, Falco Biosystems Ltd., Medical & Biological Laboratories Co., Ltd., Merus N.V., Molecular Health GmbH, Miyarisan Pharmaceutical Co., Ltd., Natera Inc., Nippon Boehringer Ingelheim Co., Ltd., Pfizer Japan Inc., Roche Diagnostics K.K., Saofi K.K., Sysmex Corp., and Taiho Pharmaceutical Co., Ltd.; grants and personal fees from Chugai Pharmaceutical Co., Ltd., MSD K.K., Ono Pharmaceutical Co., Ltd., and Takeda Pharmaceutical Co., Ltd.; and personal fees from Merck Biopharma Co., Ltd., Sumitomo Corp., and Indivumed outside the submitted work. No disclosures were reported by the other authors.

Authors' Contributions

W.Y. Pyun: Conceptualization, resources, data curation, formal analysis, supervision, funding acquisition, validation, investigation, visualization, writing–original draft, project administration, writing–review and editing. **J.H. Park:** Conceptualization, resources, data curation, formal analysis, validation, investigation, visualization, writing–original draft, writing–review and editing. **J.W. Roh:** Conceptualization, resources, data curation, investigation, visualization, methodology. **D. Jeon:** Resources, software, investigation, visualization, methodology. **J. Kim:** Resources, data curation, software, investigation, methodology. **J.E. Paik:** Resources, data curation, software, validation, investigation. **S.C. Cho:** Validation, investigation, visualization. **S.Y. Park:** Data curation, validation, investigation, visualization. **H. Lim:** Resources, data curation, software, formal analysis, validation, investigation. **H. Kim:** Resources, data curation, software, formal analysis, validation, investigation. **Y.J. Jang:** Data curation, validation, investigation, methodology. **J. Lee:** Data curation, investigation, methodology. **J.H. Byun:** Software, visualization. **D.W. Son:** Software, visualization. **S.-Y. Kim:** Conceptualization, data curation, validation, investigation. **K.-L. Guan:** Conceptualization, supervision, validation, investigation. **W.D. Lee:** Conceptualization, formal analysis, supervision, investigation. **H.Y. Gee:** Data curation, software, formal analysis, validation, investigation. **H.-W. Lee:** Resources, data curation, software, validation, investigation. **K.T. No:** Resources, data curation, software, investigation. **Y.S. Choi:** Resources, data curation, software, supervision, funding acquisition, writing–review and editing. **T. Hashimoto:** Conceptualization, supervision, funding acquisition, validation, investigation, writing–original draft, project administration, writing–review and editing. **T. Yoshino:** Conceptualization, formal analysis, supervision, funding acquisition, validation, investigation, project administration, writing–review and editing. **H.-S. Jeong:** Conceptualization, data curation, software, funding acquisition, validation, investigation, writing–original draft. **W. Namkung:** Conceptualization, formal analysis, supervision, funding acquisition, validation, investigation, project administration, writing–review and editing. **J.H. Nam:** Conceptualization, data curation, software, supervision, funding acquisition, investigation, writing–original draft, project administration, writing–review and editing. **H.W. Park:** Conceptualization, supervision, funding acquisition, project administration, writing–review and editing.

Acknowledgments

We dedicate this work to the memory of Young Ja Park, whose courage during her battle with cancer inspired this research. This work was supported by grants from the National Research Foundation of Korea (RS-2025-00556619, RS-2024-00509461, and RS-2025-18362970 to H.W. Park and 2018R1D1A1B07043856 to H.-S. Jeong) and by Korea Health Technology R&D Project through the Korea Health Industry Development Institute, funded by the Ministry of Health & Welfare, Republic of Korea (RS-2025-25459146 to H.W. Park), by Japan Agency for Medical Research and Development (24ck016971h0002 to T. Yoshino), by National Health and Medical Research Council (Ideas 2020453 to Y.S. Choi) and Cancer Council Western Australia (2022RPG0039 to Y.S. Choi), and by Brain Korea 21 FOUR Program grant (to W.Y. Pyun, S.Y. Park, S.C. Cho, and J.E. Paik).

Note

Supplementary data for this article are available at Cancer Research Online (http://cancerres.aacrjournals.org/).

Received March 12, 2025; revised July 25, 2025; accepted November 21, 2025; posted first November 25, 2025.

References

1. Vander Heiden MG. Targeting cancer metabolism: a therapeutic window opens. Nat Rev Drug Discov 2011;10:671–84.
2. Hanahan D, Weinberg RA. Hallmarks of cancer: the next generation. Cell 2011;144:646–74.
3. Dey P, Kimmelman AC, DePinho RA. Metabolic codependencies in the tumor microenvironment. Cancer Discov 2021;11:1067–81.
4. Nencioni A, Caffa I, Cortellino S, Longo VD. Fasting and cancer: molecular mechanisms and clinical application. Nat Rev Cancer 2018;18:707–19.
5. Altea-Manzano P, Cuadros AM, Broadfield LA, Fendt SM. Nutrient metabolism and cancer in the in vivo context: a metabolic game of give and take. EMBO Rep 2020;21:e50635.
6. Muir A, Vander Heiden MG. The nutrient environment affects therapy. Science 2018;360:962–3.
7. Lee C, Raffaghello L, Brandhorst S, Safdie FM, Bianchi G, Martin-Montalvo A, et al. Fasting cycles retard growth of tumors and sensitize a range of cancer cell types to chemotherapy. Sci Transl Med 2012;4:124ra27.
8. Marciano R, Prasad M, Ievy T, Tzadok S, Leprivier G, Elkabets M, et al. High-throughput screening identified compounds sensitizing tumor cells to glucose starvation in culture and VEGF inhibitors in vivo. Cancers (Basel) 2019;11:156.
9. Jacobson MP, Friesner RA, Xiang Z, Honig B. On the role of the crystal environment in determining protein side-chain conformations. J Mol Biol 2002;320:597–608.
10. Olsson MH, Søndergaard CR, Rostkowski M, Jensen JH. PROPKA3: consistent treatment of internal and surface residues in empirical pKa predictions. J Chem Theor Comput 2011;7:525–37.
11. Harder E, Damm W, Maple J, Wu C, Reboul M, Xiang JY, et al. OPLS3: a force field providing broad coverage of drug-like small molecules and proteins. J Chem Theor Comput 2016;12:281–96.
12. Halgren TA, Murphy RB, Friesner RA, Beard HS, Frye LL, Pollard WT, et al. Glide: a new approach for rapid, accurate docking and scoring. 2. Enrichment factors in database screening. J Med Chem 2004;47:1750–9.
13. Dixon SL, Smondyrev AM, Rao SN. PHASE: a novel approach to pharmacophore modeling and 3D database searching. Chem Biol Drug Des 2006;67:370–2.
14. Friesner RA, Banks JL, Murphy RB, Halgren TA, Klicic JJ, Mainz DT, et al. Glide: a new approach for rapid, accurate docking and scoring. 1. Method and assessment of docking accuracy. J Med Chem 2004;47:1739–49.
15. Alexeev Y, Mazanetz MP, Ichihara O, Fedorov DG. GAMESS as a free quantum-mechanical platform for drug research. Curr Top Med Chem 2012;12:2013–33.
16. Nishimoto Y, Fedorov DG, Irle S. Third-order density-functional tight-binding combined with the fragment molecular orbital method. Chem Phys Lett 2015;636:90–6.
17. Gaus M, Lu X, Elstner M, Cui Q. Parameterization of DFTB3/3OB for sulfur and phosphorus for chemical and biological applications. J Chem Theor Comput 2014;10:1518–37.
18. Rappé AK, Casewit CJ, Colwell K, Goddard WA III, Skiff WM. UFF, a full periodic table force field for molecular mechanics and molecular dynamics simulations. J Am Chem Soc 1992;114:10024–35.
19. Nishimoto Y, Fedorov DG. The fragment molecular orbital method combined with density-functional tight-binding and the polarizable continuum model. Phys Chem Chem Phys 2016;18:22047–61.
20. Fedorov DG, Kitaura K. Second order Møller-Plesset perturbation theory based upon the fragment molecular orbital method. J Chem Phys 2004;121:2483–90.
21. Fedorov DG, Kitaura K, Li H, Jensen JH, Gordon MS. The polarizable continuum model (PCM) interfaced with the fragment molecular orbital method (FMO). J Comput Chem 2006;27:976–85.

22. Lim H, Jin X, Kim J, Hwang S, Shin KB, Choi J, et al. Investigation of hot spot region in XIAP inhibitor binding site by fragment molecular orbital method. Comput Struct Biotechnol J 2019;17:1217–25.
23. Lim H, Chun J, Jin X, Kim J, Yoon J, No KT. Investigation of protein-protein interactions and hot spot region between PD-1 and PD-L1 by fragment molecular orbital method. Sci Rep 2019;9:1–11.
24. Goncalves MD, Hopkins BD, Cantley LC. Dietary fat and sugar in promoting cancer development and progression. Annu Rev Canc Biol 2019;3:255–73.
25. Giovannucci E, Harlan DM, Archer MC, Bergenstal RM, Gapstur SM, Habel LA, et al. Diabetes and cancer: a consensus report. Diabetes Care 2010;33:1674–85.
26. Lien EC, Westermark AM, Zhang Y, Yuan C, Li Z, Lau AN, et al. Low glycaemic diets alter lipid metabolism to influence tumour growth. Nature 2021;599:302–7.
27. Berson A, Schmets L, Fisch C, Fau D, Wolf C, Fromenty B, et al. Inhibition by nilutamide of the mitochondrial respiratory chain and ATP formation. Possible contribution to the adverse effects of this antiandrogen. J Pharmacol Exp Ther 1994;270:167–76.
28. Syed M, Skonberg C, Hansen SH. Mitochondrial toxicity of selective COX-2 inhibitors via inhibition of oxidative phosphorylation (ATP synthesis) in rat liver mitochondria. Toxicol In Vitro 2016;32:26–40.
29. Wheaton WW, Weinberg SE, Hamanaka RB, Soberanes S, Sullivan LB, Anso E, et al. Metformin inhibits mitochondrial complex I of cancer cells to reduce tumorigenesis. Elife 2014;3:e02242.
30. Graham PM, Li JZ, Dou X, Zhu H, Misra HP, Jia Z, et al. Protection against peroxynitrite-induced DNA damage by mesalamine: implications for anti-inflammation and anti-cancer activity. Mol Cell Biochem 2013;378:291–8.
31. Struwe M, Greulich KO, Perentes E, Martus HJ, Suter W, Plappert-Helbig U. Repair of sparfloxacin-induced photochemical DNA damage in vivo. J Invest Dermatol 2009;129:699–704.
32. Bolzán AD, Bianchi MS. Genotoxicity of streptozotocin. Mutat Res 2002;512:121–34.
33. Hu J, La Vecchia C, de Groh M, Negri E, Morrison H, Mery L; Canadian Cancer Registries Epidemiology Research Group. Dietary cholesterol intake and cancer. Ann Oncol 2012;23:491–500.
34. Herrmann J. Adverse cardiac effects of cancer therapies: cardiotoxicity and arrhythmia. Nat Rev Cardiol 2020;17:474–502.
35. Alexandre J, Moslehi JJ, Bersell KR, Funck-Brentano C, Roden DM, Salem JE. Anticancer drug-induced cardiac rhythm disorders: current knowledge and basic underlying mechanisms. Pharmacol Ther 2018;189:89–103.
36. Buza V, Rajagopalan B, Curtis AB. Cancer treatment-induced arrhythmias: focus on chemotherapy and targeted therapies. Circ Arrhythm Electrophysiol 2017;10:e005443.
37. Aboumsallem JP, Moslehi J, de Boer RA. Reverse cardio-oncology: cancer development in patients with cardiovascular disease. J Am Heart Assoc 2020;9:e013754.
38. Karlstaedt A, Moslehi J, de Boer RA. Cardio-onco-metabolism: metabolic remodelling in cardiovascular disease and cancer. Nat Rev Cardiol 2022;19:414–25.
39. Pullen N, Dennis PB, Andjelkovic M, Dufner A, Kozma SC, Hemmings BA, et al. Phosphorylation and activation of p70s6k by PDK1. Science 1998;279:707–10.
40. Sarbassov DD, Guertin DA, Ali SM, Sabatini DM. Phosphorylation and regulation of Akt/PKB by the rictor-mTOR complex. Science 2005;307:1098–101.
41. Hardie DG. AMP-activated protein kinase: an energy sensor that regulates all aspects of cell function. Genes Dev 2011;25:1895–908.
42. Inoki K, Zhu T, Guan KL. TSC2 mediates cellular energy response to control cell growth and survival. Cell 2003;115:577–90.
43. Shackelford DB, Shaw RJ. The LKB1-AMPK pathway: metabolism and growth control in tumour suppression. Nat Rev Cancer 2009;9:563–75.
44. Hudes G, Carducci M, Tomczak P, Dutcher J, Figlin R, Kapoor A, et al. Temsirolimus, interferon alfa, or both for advanced renal-cell carcinoma. N Engl J Med 2007;356:2271–81.
45. Rodrik-Outmezguine VS, Okaniwa M, Yao Z, Novotny CJ, McWhirter C, Banaji A, et al. Overcoming mTOR resistance mutations with a new-generation mTOR inhibitor. Nature 2016;534:272–6.
46. Dasanu CA, Clark BA 3rd, Alexandrescu DT. mTOR-blocking agents in advanced renal cancer: an emerging therapeutic option. Expert Opin Investig Drugs 2009;18:175–87.
47. Motzer RJ, Escudier B, Oudard S, Hutson TE, Porta C, Bracarda S, et al. Efficacy of everolimus in advanced renal cell carcinoma: a double-blind, randomised, placebo-controlled phase III trial. Lancet 2008;372:449–56.
48. Wu Q, Ba-Alawi W, Deblois G, Cruickshank J, Duan S, Lima-Fernandes E, et al. GLUT1 inhibition blocks growth of RB1-positive triple negative breast cancer. Nat Commun 2020;11:4205.
49. Barretina J, Caponigro G, Stransky N, Venkatesan K, Margolin AA, Kim S, et al. The cancer cell line encyclopedia enables predictive modelling of anticancer drug sensitivity. Nature 2012;483:603–7.
50. Schmitz A, Sankaranarayanan A, Azam P, Schmidt-Lassen K, Homerick D, Hänsel W, et al. Design of PAP-1, a selective small molecule Kv1.3 blocker, for the suppression of effector memory T cells in autoimmune diseases. Mol Pharmacol 2005;68:1254–70.
51. Yoo I, Ahn I, Lee J, Lee N. Extracellular flux assay (Seahorse assay): diverse applications in metabolic research across biological disciplines. Mol Cells 2024;47:100095.
52. Gross D, Bischof H, Maier S, Sporbeck K, Birkenfeld AL, Malli R, et al. IK(Ca) channels control breast cancer metabolism including AMPK-driven autophagy. Cell Death Dis 2022;13:902.
53. Oeggerli M, Tian Y, Ruiz C, Wijker B, Sauter G, Obermann E, et al. Role of KCNMA1 in breast cancer. PLoS One 2012;7:e41664.
54. Bloch M, Ousingsawat J, Simon R, Schraml P, Gasser TC, Mihatsch MJ, et al. KCNMA1 gene amplification promotes tumor cell proliferation in human prostate cancer. Oncogene 2007;26:2525–34.
55. Park JH, Shin JE, Park HW. The role of Hippo pathway in cancer stem cell biology. Mol Cells 2018;41:83–92.
56. Zhang X, Qiao Y, Wu Q, Chen Y, Zou S, Liu X, et al. The essential role of YAP O-GlcNAcylation in high-glucose-stimulated liver tumorigenesis. Nat Commun 2017;8:15280.
57. Cox AG, Tsomides A, Yimlamai D, Hwang KL, Miesfeld J, Galli GG, et al. Yap regulates glucose utilization and sustains nucleotide synthesis to enable organ growth. EMBO J 2018;37:e100294.
58. Ortillon J, Le Bail JC, Villard E, Léger B, Poirier B, Girardot C, et al. High glucose activates YAP signaling to promote vascular inflammation. Front Physiol 2021;12:665994.
59. Gormsen LC, Søndergaard E, Christensen NL, Brøsen K, Jessen N, Nielsen S. Metformin increases endogenous glucose production in non-diabetic individuals and individuals with recent-onset type 2 diabetes. Diabetologia 2019;62:1251–6.
60. Coperchini F, Leporati P, Rotondi M, Chiovato L. Expanding the therapeutic spectrum of metformin: from diabetes to cancer. J Endocrinol Invest 2015;38:1047–55.
61. Birsoy K, Possemato R, Lorbeer FK, Bayraktar EC, Thiru P, Yucel B, et al. Metabolic determinants of cancer cell sensitivity to glucose limitation and biguanides. Nature 2014;508:108–12.
62. Zhuang YX, Chan DK, Haugrud AB, Miskimins WK. Mechanisms by which low glucose enhances the cytotoxicity of metformin to cancer cells both in vitro and in vivo. PLoS One 2014;9:e108444.
63. Horie M, Saito A, Ohshima M, Suzuki HI, Nagase T. YAP and TAZ modulate cell phenotype in a subset of small cell lung cancer. Cancer Sci 2016;107:1755–66.
64. Donato E, Biagioni F, Bisso A, Caganova M, Amati B, Campaner S. YAP and TAZ are dispensable for physiological and malignant haematopoiesis. Leukemia 2018;32:2037–40.
65. Kim J, Lim H, Moon S, Cho SY, Kim M, Park JH, et al. Hot spot analysis of YAP-TEAD protein-protein interaction using the fragment molecular orbital method and its application for inhibitor discovery. Cancers (Basel) 2021;13:4246.
66. Pobbati AV, Han X, Hung AW, Weiguang S, Huda N, Chen G-Y, et al. Targeting the central pocket in human transcription factor TEAD as a potential cancer therapeutic strategy. Structure 2015;23:2076–86.
67. Tang TT, Konradi AW, Feng Y, Peng X, Ma M, Li J, et al. Small molecule inhibitors of TEAD auto-palmitoylation selectively inhibit proliferation and tumor growth of NF2-deficient mesothelioma. Mol Cancer Ther 2021;20:986–98.
68. Park JH, Pyun WY, Park HW. Cancer metabolism: phenotype, signaling and therapeutic targets. Cells 2020;9:2308.
69. Tajan M, Vousden KH. Dietary approaches to cancer therapy. Cancer Cell 2020;37:767–85.
70. Mayne ST, Playdon MC, Rock CL. Diet, nutrition, and cancer: past, present and future. Nat Rev Clin Oncol 2016;13:504–15.
71. Sullivan MR, Danai LV, Lewis CA, Chan SH, Gui DY, Kunchok T, et al. Quantification of microenvironmental metabolites in murine cancers reveals determinants of tumor nutrient availability. Elife 2019;8:e44235.

72. Vecchio E, Caiazza C, Mimmi S, Avagliano A, Iaccino E, Brusco T, et al. Metabolites profiling of melanoma interstitial fluids reveals uridine diphosphate as potent immune modulator capable of limiting tumor growth. Front Cell Dev Biol 2021;9:730726.
73. Zhang Y, Kurupati R, Liu L, Zhou XY, Zhang G, Hudaihed A, et al. Enhancing CD8(+) T cell fatty acid catabolism within a metabolically challenging tumor microenvironment increases the efficacy of melanoma immunotherapy. Cancer Cell 2017;32:377–91.e9.
74. Elgendy M, Ciro M, Hosseini A, Weiszmann J, Mazzarella L, Ferrari E, et al. Combination of hypoglycemia and metformin impairs tumor metabolic plasticity and growth by modulating the PP2A-GSK3beta-MCL-1 axis. Cancer Cell 2019;35:798–815.e5.
75. Lunt SY, Vander Heiden MG. Aerobic glycolysis: meeting the metabolic requirements of cell proliferation. Annu Rev Cell Dev Biol 2011;27:441–64.
76. Tufail M, Jiang CH, Li N. Altered metabolism in cancer: insights into energy pathways and therapeutic targets. Mol Cancer 2024;23:203.